Inorganic Chemistry

Article

pubs.acs.org/IC

3,5-Bis(ethynyl)pyridine and 2,6-Bis(ethynyl)pyridine Spanning Two Fe(Cp*)(dppe) Units: Role of the Nitrogen Atom on the Electronic and Magnetic Couplings

Karine Costuas,*[,†] Olivier Cador,[†] Frédéric Justaud,[†] Sylvie Le Stang,[†] Frédéric Paul,[†] Antonio Monari,[‡] Stefano Evangelisti,[§] Loïc Toupet,[⊥] Claude Lapinte,*[,†] and Jean-François Halet*[,†]

[†]Laboratoire des Sciences Chimiques de Rennes, UMR 6226 CNRS—Université de Rennes 1, F-35042 Rennes cedex, France

[‡]Equipe de Chimie et Biochimie Théorique, SRSMC, UMR 7565 CNRS—Université de Nancy, BP 70239, Boulevard des Aiguilettes, F-54506 Vandoeuvre-lès-Nancy cedex, France

[§]Laboratoire de Chimie et Physique Quantiques, UMR 5626, CNRS—Université Paul Sabatier de Toulouse, 118, Route de Narbonne, F-31062 Toulouse cedex 09, France

[⊥]Institut de Physique de Rennes, UMR 6251, CNRS—Université de Rennes 1, F-35042 Rennes cedex, France

Supporting Information

ABSTRACT: The role of the nitrogen atom on the electronic and magnetic couplings of the mono-oxidized and bi-oxidized pyridine-containing complex models $[2,6\text{-}\{Cp(dpe)Fe{-}C{\equiv}C{-}\}_2(NC_5H_3)]^{n+}$ and $[3,5\text{-}\{Cp(dpe)Fe{-}C{\equiv}C{-}\}_2(NC_5H_3)]^{n+}$ is theoretically tackled with the aid of density-functional theory (DFT) and multireference configuration interaction (MR-CI) calculations. Results are analyzed and compared to those obtained for the reference complex $[1,3\text{-}\{Cp^*(dppe)Fe{-}C{\equiv}C{-}\}_2(C_6H_4)]^{n+}$. The mono-oxidized species show an interesting behavior at the borderline between spin localization and delocalization and one through-bond communication path among the two involving the central ring, is favored. Investigation of the spin state of the dicationic complexes indicates ferromagnetic coupling, which can differ in magnitude from one complex to the other. Very importantly, electronic and magnetic properties of these species strongly depend not only upon the location of the nitrogen atom in the ring versus that of the organometallic end-groups but also upon the architectural arrangement of one terminus, with respect to the other and/or vis-à-vis the central ring. To help validate the theoretical results, the related families of compounds $[1,3\text{-}\{Cp^*(dppe)Fe{-}C{\equiv}C{-}\}_2(C_6H_4)]^{n+}$, $[2,6\text{-}\{Cp^*(dppe)Fe{-}C{\equiv}C{-}\}_2(NC_5H_3)]^{n+}$, $[3,5\text{-}\{Cp^*(dppe)Fe{-}C{\equiv}C{-}\}_2(NC_5H_3)]^{n+}$ (n = 0−2) were experimentally synthesized and characterized. Electrochemical, spectroscopic (infrared (IR), Mössbauer), electronic (near-infrared (NIR)), and magnetic properties (electron paramagnetic resonance (EPR), superconducting quantum interference device (SQUID)) are discussed and interpreted in the light of the theoretical data. The set of data obtained allows for many strong conclusions to be drawn. A N atom in the long branch increases the ferromagnetic interaction between the two Fe^{III} spin carriers (J > 500 cm^{-1}), whereas, when placed in the short branch, it dramatically reduces the magnetic exchange in the di-oxidized species (J = 2.14(5) cm^{-1}). In the mixed-valence compounds, when the N atom is positioned on the long branch, the intermediate excited state is higher in energy than the different ground-state conformers and the relaxation process provides exclusively the Fe^{II}/Fe^{III} localized system ($H_{ab} \neq 0$). Positioning the N atom on the short branch modifies the energy profile and the diabatic mediating state lies just above the reactant and product diabatic states. Consequently, the LMCT transition becomes less energetic than the MMCT transition. Here, the direct coupling does not occur (H_{ab} = 0) and only the coupling through the bridge (c) and the reactant (a) and product (b) diabatic states is operating ($H_{ac} = H_{bc} \neq 0$).

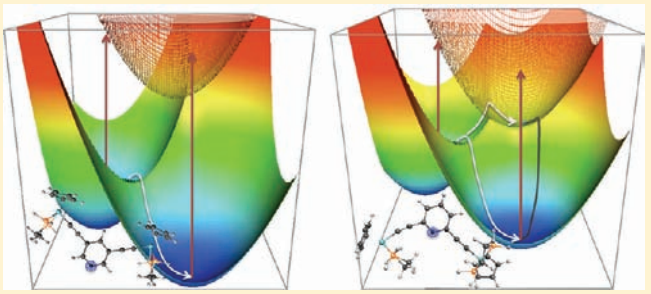

INTRODUCTION

Molecules comprised of two redox active centers connected by a carbon bridge provide an ideal template upon which intricate mechanistic details concerning the factors controlling electron transfer and electron delocalization in chemistry can be extracted.[1−5] Consequently, over the last years, one thrust has involved extremes in oxidation states of this type of compound with different metal end-groups and the consequences for electronic, magnetic, and geometric structure, as well as electron transfer, have been studied extensively.[6] We have shown that species containing redox-active Cp*(dppe)Fe fragments (Cp* = C_5Me_5, dppe =1,2-bis(diphenylphosphino)-ethane) linked to π-conjugated polyynediyl ligands such as $[Cp^*(dppe)Fe{-}C{\equiv}C{-})]_2$ (**1**; see Chart 1)[7] are ideally suited

Received: July 27, 2011
Published: November 9, 2011

Chart 1

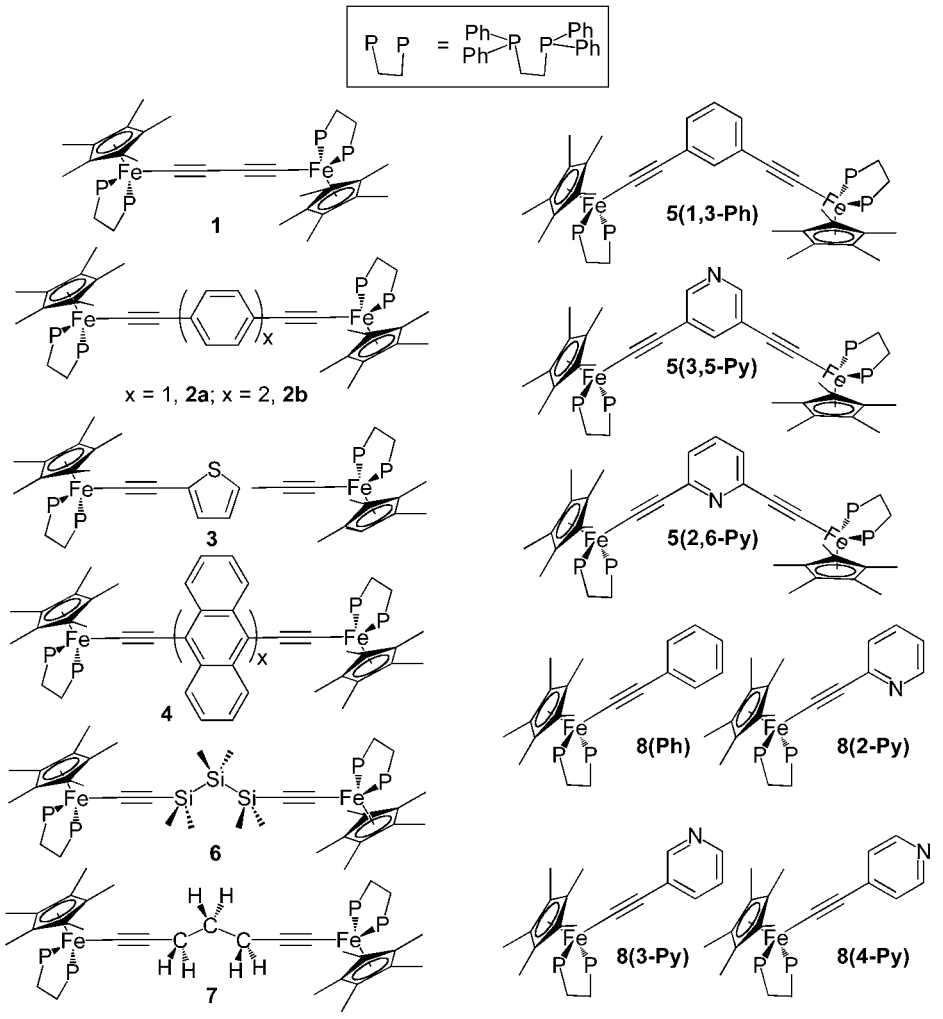

for studies of electronic and magnetic coupling between the redox centers. These assemblies usually proved to be stable (and isolable) in different redox states.[8] However, previous studies have clearly shown that the length expansion of polyynediyl linkers is limited by the poor chemical stability of the oxidized species. Introduction of aromatic rings such as benzene or thiophene in the polyynediyl spacer constitutes an attractive alternative to circumvent this instability and eventually to tune their physical properties. Various nonlinear rigid new geometries can then be envisioned for the carbon-rich spacers incorporating such aromatic units, leading to structural variation, which can deeply modify the electronic properties of the molecules.[9−14]

In their singly oxidized forms, these iron complexes are seen to traverse the Robin−Day classification of mixed-valence (MV) compounds,[15,16] from valence-trapped (Class II), where some properties of distinct, localized Fe^{II}/Fe^{III} components must be discernible under certain conditions, intermediate (Class II−III), and fully delocalized (Class III), depending upon the nature and the length of the electron-conveyor carbon bridge.[17] Thus, starting from the monocationic MV Class III compound $[Cp^*(dppe)Fe{-}C{\equiv}C{-})]_2[PF_6]$ ($\mathbf{1}^+$, Chart 1),[7] incorporation of a *meta*-phenylene entity in the butadiyne-diyl spacer leads to a weakly coupled MV or Class II complex $[1,3\text{-}\{Cp^*(dppe)Fe{-}C{\equiv}C{-})\}_2(C_6H_4)][PF_6]$ [**5(1,3-Ph)**][**PF_6**].[9,10] On the other hand, insertion of a *para*-phenylene ring in $[1,4\text{-}\{Cp^*(dppe)Fe{-}C{\equiv}C{-})\}_2(C_6H_4)][PF_6]$ ($\mathbf{2a}^+$) produces a smooth "delocalized" Class III to borderline Class II−III transition.[11] Interestingly, subsequent addition of a *para*-phenylene unit in $[\{Cp^*(dppe)Fe\}_2(C{\equiv}C\text{-}4,4'\text{-}\{1,1'\text{-}(C_6H_4)_2\}C{\equiv}C)][PF_6]$ ($\mathbf{2b}^+$) results in an MV Class II complex.[11] Strongly coupled Class III systems can be obtained instead if thiophene or anthracene are inserted in the carbon bridge as exemplified with $[2,5\text{-}\{Cp^*(dppe)Fe{-}C{\equiv}C{-})\}_2(SC_4H_2)][PF_6]$ ($\mathbf{3}^+$) and $[9,10\text{-}\{Cp^*(dppe)Fe{-}C{\equiv}C{-})\}_2(C_{14}H_8)][PF_6]$ ($\mathbf{4}^+$).[12,13]

Further oxidation generally yields stable dicationic species, which are diagmagnetic, antiferromagnetic, ferromagnetic, exist as a mixture of low-spin (S = 0) and high-spin (S = 1) isomers in equilibrium at room temperature, also depending upon the length and the nature of the carbon bridge. For instance, magnetic susceptibility measurements on dicationic $[Cp^*(dppe)Fe{-}C{\equiv}C{-}]_2[PF_6]_2$ ($\mathbf{1}^{2+}$) suggest that both low and high spin states are populated, even at liquid nitrogen temperature, whereas dicationic species $[1,3\text{-}\{Cp^*(dppe)Fe{-}C{\equiv}C{-}\}_2(C_6H_4)][PF_6]_2$ [**5(1,3-Ph)**][**PF_6**]$_2$ and $[1,4\text{-}\{Cp^*(dppe)Fe{-}C{\equiv}C{-}\}_2(C_6H_4)][PF_6]_2$ ($\mathbf{2a}^{2+}$) incorporating *meta*- and *para*-substituted aryl groups, respectively, revealed a ferromagnetic and antiferromagnetic coupling in the ground state, respectively.[18] Antiferromagnetic exchange interaction between the two iron spin carriers is also observed for $[2,5\text{-}\{Cp^*(dppe)Fe{-}C{\equiv}C{-}\}_2(SC_4H_2)][PF_6]_2$ ($\mathbf{3}^{2+}$) containing

dx.doi.org/10.1021/ic2016148 | *Inorg. Chem.* 2011, 50, 12601−12622

thiophene.[19] In contrast, [9,10-{Cp*(dppe)Fe−C≡C−}$_2$($C_{14}H_8$)][PF_6]$_2$ ($\mathbf{4}^{2+}$) is diamagnetic with a large energy gap between the singlet ground state and the triplet excited state.[13]

Obviously, various bridging groups, but also different ligand topology (*meta* vs *para* for instance), can mediate in different manners electronic interactions between structurally identical redox metal sites.[20] The coupling between the two metal end-groups can occur directly via a through-bond mechanism, or indirectly via a through-space superexchange process.[16] If we assume that, in the above-mentioned mixed-valence cationic species, there is some through-bond electron transfer from the Fe^{II} center to the Fe^{III} center, an electronic path is necessary along the bridge. In the case of the Class II mixed-valence complex [1,3-{Cp*(dppe)Fe−C≡C−}$_2$(C_6H_4)][PF_6] [**5(1,3-Ph)**][PF_6], two different paths—a short one or a long one in the phenylene ring—can be envisaged. A destructive interference may even occur if there is some "crosstalk" between the two paths.[21] The path for such a connection between the two metal centers in this molecule is still not completely understood. What would happen if a heteroatom were inserted in the phenyl ring? We may think that the substitution of a CH group by a N atom, for instance, either in the short branch or in the long branch may give some indirect information about the electron path which prevails in [**5(1,3-Ph)**]$^+$.

This paper reports theoretical and experimental results obtained on the nitrogen-substituted [2,6-{Cp*(dppe)Fe−C≡C−}$_2$(NC_5H_3)]$^{n+}$ [**5(2,6-Py)**]$^{n+}$, *ortho*−*ortho*′ isomer), [3,5-{Cp*(dppe)Fe−C≡C−}$_2$(NC_5H_3)]$^{n+}$ [**5(3,5-Py)**]$^{n+}$, *meta*−*meta*′ isomer) compounds (n = 0−2) as well as the reference [1,3-{Cp*(dppe)Fe−C≡C−}$_2$(C_6H_4)]$^{n+}$ [**5(1,3-Ph)**]$^{n+}$ compound,[9] which are used to analyze how the N atom enhances or diminishes the electronic and magnetic couplings between the iron end-groups connected in meta positions.

WHAT DOES THE THEORY SAY (OR NOT SAY)?

Density functional theory (DFT) and multireference configuration interaction (MR-CI) calculations were carried out prior to experiments, on the neutral and oxidized pyridine-containing models [2,6-{Cp(dpe)Fe−C≡C−}$_2$(NC_5H_3)]$^{n+}$ [**5H(2,6-Py)**]$^{n+}$, ortho isomer), [3,5-{Cp(dpe)Fe−C≡C−}$_2$(NC_5H_3)]$^{n+}$ [**5H(3,5-Py)**]$^{n+}$, meta isomer) (dpe = H_2P−(CH_2)$_2$−PH_2); Cp = η^5-C_5H_5; n = 0−2) (see Scheme 1)

Scheme 1. Computed Complex Models with Atom Labeling

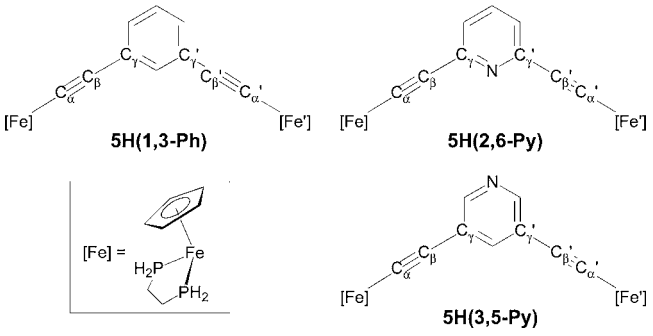

that employ Cp(dpe)Fe fragments (Cp = C_5H_5 and dpe = bis(phosphino)ethane) rather than Cp*(dppe)Fe moieties to reduce the computational effort. For the sake of comparison, calculations were performed again on the previously studied theoretical model [1,3-{Cp(dpe)Fe−C≡C−}$_2$(C_6H_4)]$^{n+}$ [**5H-(1,3-Ph)**]$^{n+}$ (Scheme 1) at the same level of theory.[9]

Optimized Geometries and Energies. Pertinent metrical optimized data for [**5H(2,6-Py)**]$^{n+}$, [**5H(3,5-Py)**]$^{n+}$, and [**5H(1,3-Ph)**]$^{n+}$ (n = 0−2) series are reported in Table 1. Introducing a heteroatom in the conjugated bridge hardly affects the atomic distances and angles in the backbone of the molecules. Fe−C, ethynyl C−C, and ring C−C bonds are comparable, within the range of a few thousandths of an Angstrom (Å)), in both neutral and oxidized species. They are entirely consistent with values generally measured for this type of complex.[22]

As observed in related compounds,[23] subsequent oxidation implies some change in the atomic bond lengths in the molecular backbones (i.e., some shortening of the Fe−C(ethynyl) bonds and a slight lengthening of the ethynyl C−C bonds (see Table 1)). Some asymmetry being experimentally noted in the X-ray structure of [**5(1,3-Ph)**][PF_6] (vide infra), different symmetrical and asymmetrical monocationic model species were tentatively computed and compared. Consequently, symmetrical (reflecting complete delocalization) and asymmetrical (reflecting only partial delocalization) geometries were considered for the mixed-valence mono-oxidized species [**5H(2,6-Py)**]$^+$, [**5H(3,5-Py)**]$^+$, and [**5H(1,3-Ph)**]$^+$.

A word about symmetrical versus asymmetrical geometries within DFT calculations is necessary here. DFT computations are often described as favoring the former over the latter. Indeed, this is true, to a certain extent, if we only consider the computed total energy. This is mainly attributed to problems of self-interaction inherent to the method.[24−26] Hybrid functionals such as B3LYP containing some Hartree−Fock (HF) exchange can then be used to try to overcome this problem.[24,27] Nevertheless, it turns out that geometry optimizations of asymmetrical arrangements are not straightforward to compute, often leading authors to conclude that DFT favors symmetrical arrangements. Most of the DFT quantum chemistry programs provide initial electronic density guesses that are not well-suited to handle asymmetrical geometry calculations, since they are simply the addition of atomic densities. One must introduce a symmetry breaking in the initial geometry as well as in the electronic density to tentatively obtain an asymmetrical solution. On this basis, we performed calculations on cationic models with asymmetrical starting geometries and electronic densities (the two Fe atoms were deliberately distinguished as Fe^{II} and Fe^{III} (see the Computational Details section)). Let us add that when this method fails, one can "force" localization of the spin-density by employing the constrained DFT (CDFT) formalism proposed by Wu and Van Voorhis;[28] however, the result is dependent on the choice of the constraints and must be used with caution. This method was recently successfully applied to [**5H(1,3-Ph)**]$^+$.[10]

Interestingly, the computations that we performed led to asymmetrical systems that were very close in energy (separated by less than 0.06 eV (6 kJ/mol)) to the symmetrical optimized geometries (compare [**5H(2,6-Py)**]^+_s, [**5H(3,5-Py)**]^+_s, and [**5H(1,3-Ph)**]^+_s, and [**5H(2,6-Py)**]$^+_{as1}$, [**5H(3,5-Py)**]$^+_{as}$, and [**5H(1,3-Ph)**]$^+_{as1}$, respectively, in Table 1). These structures proved to be energy minima by vibrational frequency calculations. The oxidation-state coloring Fe^{II}/Fe^{III} in the asymmetrical structures, indeed, is reflected in the rather important difference (ca. 0.05 Å) between the two Fe−C(α) bond lengths. In turn, the Fe^{II}−C(α) and Fe^{III}−C(α) distances, ca. 1.90 and 1.85 Å, respectively, are almost identical to those

dx.doi.org/10.1021/ic2016148 | Inorg. Chem. 2011, 50, 12601−12622

Table 1. Pertinent Optimized Bond Lengths, Relative Energies, and Adiabatic Ionization Potentials for the Models [2,6-{Cp(dpe)Fe−C≡C−}$_2$(NC$_5$H$_3$)]$^{n+}$ [5H(2,6-Py)]$^{n+}$, [3,5-{Cp(dpe)Fe−C≡C−}$_2$(NC$_5$H$_3$)]$^{n+}$ [5H(3,5-Py)]$^{n+}$, and [1,3-{Cp(dpe)Fe−C≡C−}$_2$(C$_6$H$_4$)]$^{n+}$ [5H(1,3-Ph)]$^{n+}$ (n = 0−2)[a]

	Optimized Bond Lengths (Å)							
complex	Fe−C(α)	C(α)−C(β)	C(β)−C(γ)	Fe−P[b]	Fe−C(Cp)	θ (deg)[c]	relative energy, E_{rel} (eV)	adiabatic ionization potential, IP (eV)
5H(2,6-Py)	1.904	1.237	1.436	2.209	2.139	−1	0.00	
	1.904	1.237	1.436	2.208	2.138	$\perp^2\perp^2$		
5(2,6-Py)[d]	*1.887(5)*	*1.219(6)*	*1.426(6)*	2.174				
	1.886(4)	*1.217(5)*	*1.413(5)*	2.177				
[**5H(2,6-Py)**]^+_s	1.854	1.245	1.424	2.231	2.143	0	5.50	
	1.854	1.245	1.424	2.231	2.143	$\perp^1\perp^1$		
[**5H(2,6-Py)**]$^+_{as1}$	1.848	1.240	1.431	2.272	2.153	7	5.46	
	1.893	1.241	1.426	2.213	2.142	$\perp^2\perp^2$		
[**5H(2,6-Py)**]$^+_{as2}$	1.858	1.245	1.422	2.224	2.143	−106	5.45	5.45
	1.850	1.240	1.423	2.234	2.144	$\perp^2$ //		
[**5H(2,6-Py)**]$^{2+}$ LS	1.815	1.255	1.413	2.253	2.147	−177	14.25	
	1.818	1.255	1.413	2.254	2.147	$\perp^1\perp^1$		
[**5H(2,6-Py)**]$^{2+}$ HS	1.873	1.238	1.439	2.278	2.158	−20	13.02	7.57
	1.874	1.238	1.439	2.279	2.157	$\perp^2\perp^2$		
[**5H(2,6-Py)**]$^{2+}$ BS	1.871	1.238	1.438	2.283	2.158	−95	13.03	
	1.879	1.237	1.443	2.288	2.159	$\perp^2$//		
5H(3,5-Py)	1.908	1.238	1.432	2.207	2.140	0	0.00	
	1.908	1.238	1.432	2.207	2.140	$\perp^2\perp^2$		
5(3,5-Py)[d]	*1.897(4)*	*1.210(5)*	*1.425(5)*	*2.184*				
	1.884(4)	*1.230(5)*	*1.433(5)*	*2.178*				
[**5H(3,5-Py)**]^+_s	1.859	1.245	1.419	2.233	2.144	0	5.48	5.48
	1.859	1.245	1.419	2.233	2.144	$\perp^2\perp^2$		
[**5H(3,5-Py)**]$^+_{as}$	1.848	1.240	1.431	2.258	2.151	101	5.54	
	1.893	1.241	1.426	2.214	2.141	$\perp^2$ //		
[**5H(3,5-Py)**]$^{2+}$ LS	1.823	1.255	1.411	2.256	2.147	−46	14.34	
	1.823	1.255	1.411	2.256	2.147	$\perp^2\perp^2$		
[**5H(3,5-Py)**]$^{2+}$ HS	1.872	1.240	1.429	2.284	2.158	0	12.95	7.47
	1.872	1.240	1.429	2.284	2.158	$\perp^2\perp^2$		
[**5H(3,5-Py)**]$^{2+}$ BS	1.876	1.239	1.430	2.284	2.158	13	12.96	
	1.874	1.239	1.430	2.286	2.158	$\perp^2\perp^2$		
5H(1,3-Ph)	1.911	1.237	1.436	2.204	2.140	91[e]	0.00	
	1.911	1.237	1.436	2.204	2.140			
5(1,3-Ph)[d]	*1.880(9)*	*1.230(11)*	*1.437(11)*	*2.175*				
	1.900(8)	*1.231(10)*	*1.411(10)*	*2.155*				
[**5H(1,3-Ph)**]^+_s	1.860	1.245	1.421	2.230	2.144	−1	5.34	5.34
	1.860	1.245	1.421	2.230	2.144	$\perp\perp$		
[**5H(1,3-Ph)**]$^+_{as1}$	1.842	1.246	1.420	2.213	2.151	−93	5.40	
	1.895	1.241	1.425	2.244	2.141	$\perp$ //		
[**5H(1,3-Ph)**]$^+_{as2}$	1.847	1.246	1.420	2.241	2.148	170	5.35	
	1.878	1.243	1.422	2.220	2.143	$\perp\perp$		
[**5H(1,3-Ph)**]$^+_{as3}$	1.857	1.246	1.420	2.227	2.144	−28	5.39	
	1.862	1.246	1.421	2.224	2.143	$\perp\perp$		
[**5(1,3-Ph)**]$^+$ [d,f]	*1.877(13)*	*1.204(15)*	*1.451(14)*	*2.230*		*−121*		
	1.880(11)	*1.193(14)*	*1.424(16)*	*2.254*				
[**5H(1,3-Ph)**]$^{2+}$ LS	1.823	1.255	1.412	2.254	2.148	0	14.05	
	1.823	1.255	1.412	2.254	2.148	$\perp\perp$		
[**5H(1,3-Ph)**]$^{2+}$ HS	1.867	1.240	1.431	2.282	2.157	0	12.72	7.38
	1.867	1.240	1.431	2.282	2.157	$\perp\perp$		
[**5H(1,3-Ph)**]$^{2+}$ BS	1.870	1.240	1.432	2.282	2.158	176	12.78	
	1.871	1.240	1.432	2.276	2.157	$\perp\perp$		

[a]For atom labeling, see Scheme 1. Crystallographic data for corresponding complexes are given when available. [b]Average distance. [c]As defined in Chart 2. [d]Only one of the two independent molecules is reported here. [e]The metallic fragments strongly deviate from the parallel or perpendicular mode with the centroid (P−P)−Fe−Ph dihedral angles of −47° and −32°. [f]From ref 9.

computed for the monometallic analogues: {Cp(PH$_3$)$_2$Fe^{II}}-(C≡C−C$_6$H$_5$) on one hand and [{Cp(PH$_3$)$_2$Fe^{III}}(C≡C−C$_6$H$_5$)]$^+$ on the other hand (Fe−C(α) = 1.91 Å and 1.85 Å, respectively).[29] As expected for this type of complex, the

dx.doi.org/10.1021/ic2016148 | Inorg. Chem. 2011, 50, 12601−12622

Fe−C(α) bond lengths computed for the symmetrical cationic geometries (ca. 1.86 Å) are ca. 0.05 Å shorter than those computed for the neutral models. Note that the ethynyl C−C distances are similar in both symmetrical and asymmetrical cationic geometries.

The electronic properties of the {Cp(dpe)Fe} (or {Cp*(dppe)Fe}) fragment are typical of that of a square-based pyramidal pseudo-ML_5 fragment.[30] Because of the reduction in symmetry, due to the different nature of the ancillary ligands, the well-known "t_{2g}" set of orbitals of a C_{4v} ML_5 fragment is modified and the two dπ orbitals become slightly different in symmetry, energy, and shape. This implies different interactions of the latter with the π frontier orbitals of the bridging carbon ligand. Consequently, the orientation of the metallic fragments, with respect to each other and with respect to the aromatic ring, is very important. Combinations of three orientations for each metallic fragment depicted in Chart 2

Chart 2

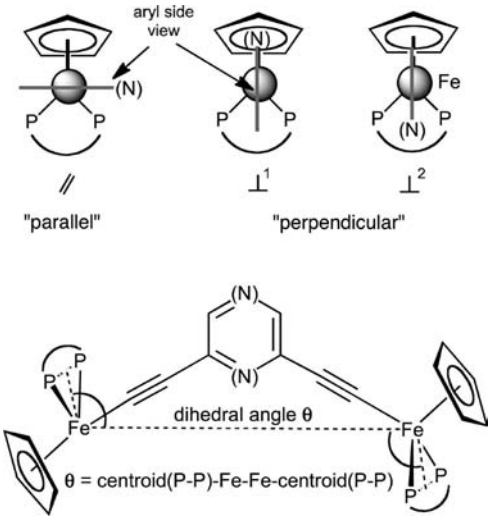

were chosen as starting geometries. Interestingly, in the case of $[\mathbf{5H(3,5\text{-}Py)}]^+$, the final (optimized) geometry found was that previously computed and reported in Table 1 as $[\mathbf{5H(3,5\text{-}Py)}]^+_s$, whereas an additional energy minimum was found in the case of $[\mathbf{5H(2,6\text{-}Py)}]^+$ for a slightly asymmetrical geometry $[\mathbf{5H(2,6\text{-}Py)}]^+_{as2}$, i.e., with two Fe−C($\alpha$) bond separations differing by only 0.008 Å. The conformational study of $[\mathbf{5H(1,3\text{-}Ph)}]^+$ led to a few stable structures. Actually, in addition to the symmetric and asymmetric structures initially found, two other energy minima, $[\mathbf{5H(1,3\text{-}Ph)}]^+_{as2}$ and $[\mathbf{5H(1,3\text{-}Ph)}]^+_{as3}$, were found 0.01 and 0.05 eV (1 and 5 kJ/mol, respectively) less stable than $[\mathbf{5H(1,3\text{-}Ph)}]^+_s$ (see Table 1). These structures differ by the value of the dihedral angle θ and the orientation of the metallic moieties {Cp(dpe)Fe}, with respect to the phenyl plane, which are of 170° (⊥ ⊥) for $[\mathbf{5H(1,3\text{-}Ph)}]^+_{as2}$ and −28° (⊥ ⊥) for $[\mathbf{5H(1,3\text{-}Ph)}]^+_{as3}$. The difference between the two Fe−C(α) distances is indeed affected by these conformational changes (0.031 Å and 0.009 Å, respectively). Indeed, this indicates that the potential energy surface of these cationic species is quite flat, with respect to the rotation of the metallic end-groups, which is accompanied by some change in the metal-bridge bond lengths.

The geometries of the dicationic forms of **5H(2,6-Py)**, **5H(3,5-Py)**, and **5H(1,3-Ph)** were also investigated. Indeed, three different spin states were investigated, i.e., the closed-shell singlet (low-spin (LS) diamagnetic state), the triplet state (high-spin (HS) magnetic state), and the broken symmetry singlet (BS antiferromagnetic state).[31] Pertinent atomic separations associated to these different magnetic states for $[\mathbf{5H(2,6\text{-}Py)}]^{2+}$, $[\mathbf{5H(3,5\text{-}Py)}]^{2+}$, and $[\mathbf{5H(1,3\text{-}Ph)}]^{2+}$ are compared in Table 1. The HS and BS geometries hardly differ with Fe−C(α) and C(α)−C(β) distances of ca. 1.87 and 1.24 Å, respectively. On the other hand, the geometries corresponding to the LS state shows somewhat different structures. For the three compounds, the metal−carbon and ethynyl C−C distances are overall, 0.05 Å shorter and <0.02 Å longer than the corresponding bond lengths in the HS and BS systems. These LS structures are probably not representative of the experimental dicationic systems, since they lie much higher in energy than the HS and BS geometries (by 1.2−1.4 eV (115−135 kJ/mol)).

The energy difference between the triplet state and the BS singlet state is associated to the exchange magnetic coupling (J). Recently, Nair and co-workers have commented about different formulas related to the calculation of J within the broken-symmetry approach.[32] Based on their work, we chose to use the formulas proposed by Yamaguchi et al.[33] and Ruiz et al.,[25,34] which indeed lead to the same result. It turns out that the value of the $\hat{S}^2$ operator of the broken symmetry singlet state is really close to 1 in all cases, leading to the expression $J = E^{BS} - {}^3E^{HS}$. The exchange magnetic coupling calculated with this formula gives, respectively, a ferromagnetic interaction of 88 cm^{-1} (ca. 0.01 eV), 91 cm^{-1} (ca. 0.01 eV), and 512 cm^{-1} (ca. 0.06 eV) for $[\mathbf{5H(2,6\text{-}Py)}]^{2+}$, $[\mathbf{5H(3,5\text{-}Py)}]^{2+}$, and $[\mathbf{5H(1,3\text{-}Ph)}]^{2+}$, respectively. Therefore, at first sight, calculations seem to indicate that the presence of a heteroatom in the organic bridge should strongly lower the ferromagnetic interaction, regardless of its position.

Vibrational Spectra. The energies of the frequencies of the ethynyl C≡C vibrator are given in Table 2 for the three model compounds $[\mathbf{5H(2,6\text{-}Py)}]^{n+}$, $[\mathbf{5H(3,5\text{-}Py)}]^{n+}$, and $[\mathbf{5H(1,3\text{-}Ph)}]^{n+}$ (n = 0−2). The simulated infrared (IR) spectra for the monocationic species are shown in Figure 1. For all the neutral systems, two frequencies centered at ∼2050 cm^{-1}, which overlap to give a single absorption band in the simulated IR spectra, are computed. They are well-separated energetically from the rest of the other vibrations and are attributed to the C≡C stretching. Indeed, their analysis reveals that these two vibrational frequencies involve not only symmetrical (S) and antisymmetrical (AS) motions of the C atoms of the ethynyl groups but also, to a smaller extent, atoms of the central ring. These corresponding vibrational modes S and AS are sketched in Scheme 2. For **5H(3,5-Py)** for instance, the less-energetic mode (2049 cm^{-1}) is antisymmetrical, with respect to the two ethynyl groups, whereas the second mode (2054 cm^{-1}), less intense, is symmetrical.

As expected, less-energetic vibrational frequencies are computed for the ethynyl groups upon oxidation. Indeed, for the cationic systems with symmetrical geometries (vide supra), two modes, symmetrical and antisymmetrical, are computed in the range of 1965−1990 cm^{-1} (see Table 2). A look at their intensity indicates that the active mode is the antisymmetrical one, leading to one strong ν(C≡C) absorption band in the corresponding calculated IR spectrum (see Figure 1). As mentioned earlier, a slightly asymmetrical structure, [**5(2,6-**

dx.doi.org/10.1021/ic2016148 | Inorg. Chem. 2011, 50, 12601−12622

Table 2. Selected Calculated Vibrational Frequencies[a] for Models $[5H(2,6\text{-Py})]^{n+}$, $[5H(3,5\text{-Py})]^{n+}$, and $[5H(1,3\text{-Ph})]^{n+}$ and Experimental IR Data for the Corresponding Complexes $[5(2,6\text{-Py})][PF_6]_n$, $[5(3,5\text{-Py})][PF_6]_n$, and $[5(1,3\text{-Ph})][PF_6]_n$

compd	$\nu 1_{C\equiv C}$ (cm^{-1})	$\nu 2_{C\equiv C}$ (cm^{-1})	$\nu 1$ intensity (km mol^{-1})	$\nu 2$ intensity (km mol^{-1})	$\nu 1$ mode[b]	$\nu 2$ mode[b]	ν_{exp} (KBr)	ν_{exp} (CH_2Cl_2)
5H(2,6-Py)	2051	2056	*752*	*195*	AS	S	2045	2043
$[5H(2,6\text{-Py})]^{+}_{s}$	1975	1992	*32*	*1118*	S	AS		
$[5H(2,6\text{-Py})]^{+}_{as1}$	1978	2034	*2445*	*1730*	S	AS		
$[5H(2,6\text{-Py})]^{+}_{as2}$	1971	1993	*945*	*2016*	S	AS	1948/1987/2037	1988/2006/2035
$[5H(2,6\text{-Py})]^{2+}$ HS	1999	2002	*743*	*104*	AS	S	1945	1950
$[5H(2,6\text{-Py})]^{2+}$ BS	2006	2025	*425*	*16*	S	AS		
5H(3,5-Py)	2049	2054	*639*	*91*	AS	S	2040/2034	2044
$[5H(3,5\text{-Py})]^{+}_{s}$	1977	1979	*157*	*8943*	S	AS	1941/2042	1941/2041
$[5H(3,5\text{-Py})]^{+}_{as}$	1962	2025	*2117*	*4076*	S	AS		
$[5H(3,5\text{-Py})]^{2+}$ HS	1993	1994	*997*	*117*	AS	S	1944	1951
$[5H(3,5\text{-Py})]^{2+}$ BS	1995	2008	*1048*	*110*	AS	S		
5H(1,3-Ph)	2051	2054	*416*	*65*	AS	S		2049
$[5H(1,3\text{-Ph})]^{+}_{s}$	1965	1980	*20072*	*55*	AS	S		1998/2044
$[5H(1,3\text{-Ph})]^{+}_{as1}$	1957	2024	*1454*	*4529*	S	AS		
$[5H(1,3\text{-Ph})]^{+}_{as2}$	1961	1993	*854*	*15636*	S	AS		
$[5H(1,3\text{-Ph})]^{+}_{as3}$	1962	1979	*18105*	*1154*	S	AS		
$[5H(1,3\text{-Ph})]^{2+}$ HS	1985	1986	*1400*	*185*	AS	S		2006
$[5H(1,3\text{-Ph})]^{2+}$ BS	1983	1998	*1634*	*157*	AS	S		

[a] A scaling factor of 0.9521 was applied on vibrational frequencies (see ref 35). [b] For AS and S Modes, see Scheme 2.

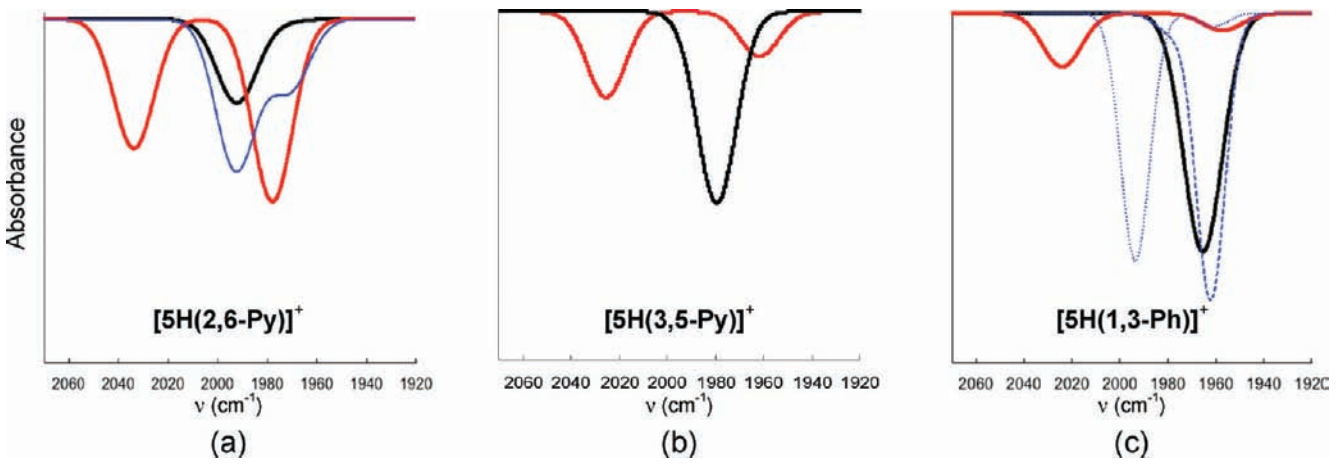

Figure 1. Simulated IR spectra of (a) $[5H(2,6\text{-Py})]^{+}_{s}$ (black), $[5H(2,6\text{-Py})]^{+}_{as1}$ (red), and $[5H(2,6\text{-Py})]^{+}_{as2}$ (blue); (b) $[5H(3,5\text{-Py})]^{+}_{s}$ (black) and $[5H(3,5\text{-Py})]^{+}_{as}$ (red); (c) $[5H(1,3\text{-Ph})]^{+}_{s}$ (black), $[5H(1,3\text{-Ph})]^{+}_{as1}$ (red), $[5H(1,3\text{-Ph})]^{+}_{as2}$ (blue, dotted line), and $[5H(1,3\text{-Ph})]^{+}_{as3}$ (blue, dashed line). The half-width coefficient of the Gaussian curves is 10.

Scheme 2. Pertinent Symmetric and Asymmetric Vibrational Modes in Pyridynyl Complexes

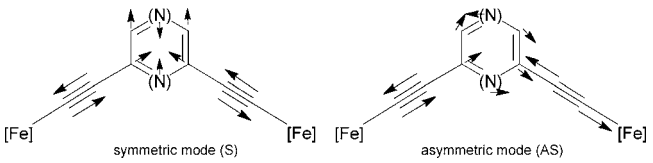

$Py)]^{+}_{as2}$ intermediate between $[5H(2,6\text{-Py})]^{+}_{s}$ and $[5H(2,6\text{-Py})]^{+}_{as1}$, is computed. This small breaking of symmetry, with respect to $[5H(2,6\text{-Py})]^{+}_{s}$, leads to a very tiny change of a couple of wavenumbers of the energies of the frequencies (Table 2), but strongly affects their intensity since the symmetrical mode becomes much more intense, leading to the appearance of a second absorption band in the IR spectra (see blue curve in the top right of Figure 1).

For the three asymmetrical structures of $[5H(1,3\text{-Ph})]^{+}_{as1/as2/as3}$, the same conclusion is drawn. The energies of the vibrations associated to the combined C≡C stretching modes are only slightly affected, compared to those found in $[5H(1,3\text{-Ph})]^{+}_{s}$ (1961 and 1962 cm^{-1} vs 1965 cm^{-1} for the first vibration and 1993 and 1979 cm^{-1} vs 1980 cm^{-1} for the second one), but the absorbances are notably affected by the rotation of one metal end-group, with respect to the other (see Figure 1c).

Two active ν(C≡C) modes, different in motion of those computed for the previous geometries and separated by 56, 63, and 67 cm^{-1} are computed for the asymmetrical geometries $[5H(2,6\text{-Py})]^{+}_{as1}$, $[5H(3,5\text{-Py})]^{+}_{as}$, and $[5H(1,3\text{-Ph})]^{+}_{as1}$,

dx.doi.org/10.1021/ic2016148 | Inorg. Chem. 2011, 50, 12601–12622

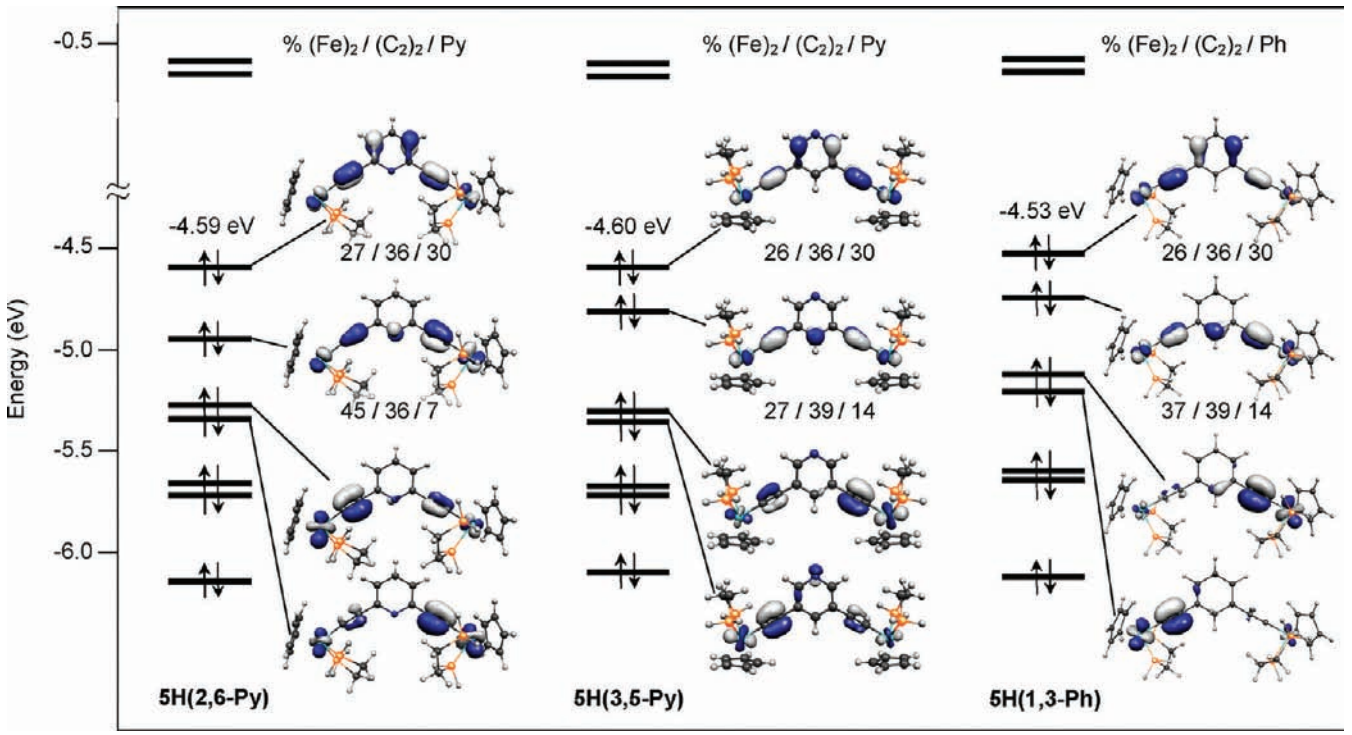

Figure 2. Frontier MO diagrams of **5H(2,6-Py)**, **5H(3,5H-Py)**, and **5H(1,3-Ph)**. The metal/ethynyl/ring contributions are given. Contour values are ± 0.035 $(e/bohr^3)^{1/2}$.

respectively (see Table 2 and the red curves on the top of Figure 1). Interestingly, one frequency (ca. 2030 cm^{-1}) is close to those computed for the neutral Fe^{II} species, the other one (ca. 1960 cm^{-1}) being close to those computed for the dicationic Fe^{III} species. Indeed, on the basis of the small energy differences between some of the conformers, one can expect that two (symmetrical and asymmetrical)—even three, in the case of **5H(2,6-Py)**, and four, in the case of $[$**5H(1,3-Ph)**$]^+$—arrangements could be found in solution simultaneously. To the best of our knowledge, this section details, for the first time, the relationship between rotational motions and spin localization, leading to "finger-print" vibrational frequencies.

Two vibrational frequencies close in energy and centered at ~2000 cm^{-1}, are also computed for the dicationic species (see Table 2). Both are of moderate intensity, with that corresponding to the antisymmetrical mode slightly more intense than the symmetrical one. It is noteworthy that the energy and intensity of these vibrations are similar for the HS and BS geometries. A glance at solely the IR spectra does not allow one to distinguish the triplet state from the singlet state of these systems.

Electronic Structures, Ionization Potentials, and Spin Densities. The MO diagrams of **5H(2,6-Py)**, **5H(3,5-Py)**, and **5H(1,3-Ph)** are compared in Figure 2. They all present a large highest occupied molecular orbital–lowest unoccupied molecular orbital (HOMO–LUMO) gap characteristic of electronically saturated molecules, i.e., with the Fe atoms obeying the 18-electron rule. As previously described elsewhere,[7,14] the energy and nodal properties of the two HOMOs of these systems are important in the description of the geometrical and physical properties of these molecules upon oxidation. They are heavily localized on the Fe centers and the ethynyl groups and to a lesser extent on the central ring. They are, in turn, mainly Fe–C(α) π-antibonding and C(α)–C(β) π-bonding in character. Consequently, successive oxidation of **5H(2,6-Py)**, **5H(3,5-Py)**, and **5H(1,3-Ph)** leads to a slight shortening of Fe–C(α) and a slight lengthening of C(α)–C(β) (vide supra).

As expected, the energy of the HOMO slightly decreases upon substitution of a C–H moiety in the central ring by the more-electronegative N atom. The metal character in the HOMOs is almost the same for the three systems; the energy difference of the HOMO levels is due to the electrostatic effects. This phenomenon has been reported earlier for the parent halide series.[36] Although the Koopmans approximation is not valid within the DFT approach, the first ionization potentials (IP) should follow the order of the energy of the HOMOs. This is effectively the case with **5H(1,3-Ph)** easier to oxidize than **5H(2,6-Py)** and **5H(3,5-Py)**, since their calculated ionization potentials are 5.34 eV, 5.45 and 5.48 eV, respectively.

The atomic spin densities of the mixed-valence $[$**5H(2,6-Py)**$]^+$, $[$**5H(3,5-Py)**$]^+$, and $[$**5H(1,3-Ph)**$]^+$ models are reported in Table 3. A three-dimensional description of the localization of the unpaired electron in these monocationic species is given in Figure 3, for their symmetrical (fully delocalized) and asymmetrical (valence trapped) forms, which are almost isoenergetic (see above). The analysis of these data should give some insight on the localization of the unpaired electron (metal centers vs carbon bridge), as well as some indication about the electron transfer pathways. In the former, the spin density is mainly localized on the Fe centers (0.65 electrons (e) for $[$**5H(2,6-Py)**$]^+_s$ and $[$**5H(3,5-Py)**$]^+_s$, and 0.60 e for $[$**5H(1,3-Ph)**$]^+_s$). In the valence-trapped structures, the unpaired electron is quasi-exclusively found on one Fe center (0.88, 0.78, and

dx.doi.org/10.1021/ic2016148 | Inorg. Chem. 2011, 50, 12601–12622

Table 3. Calculated Atomic Spin Densities for $[5H(2,6\text{-Py})]^{n+}$, $[5H(3,5\text{-Py})]^{n+}$, and $[5H(1,3\text{-Ph})]^{n+}$ (n = 1 and 2)

complex	Fe	Fe′	C(α)	C(α)′	C(β)	C(β)′	X(1)[a]	C(2)	C(3)	C(4)	C(5)	C(6)
$[5H(2,6\text{-Py})]^{+}_{s}$	+0.32	+0.32	+0.00	+0.00	+0.12	+0.12	−0.01	−0.05	+0.20	−0.08	+0.20	−0.05
$[5H(2,6\text{-Py})]^{+}_{as1}$	+0.88	+0.01	−0.09	+0.00	+0.21	+0.01	+0.02	−0.05	+0.11	−0.05	+0.11	−0.02
$[5H(2,6\text{-Py})]^{+}_{as2}$	+0.24	+0.41	+0.01	−0.01	+0.10	+0.14	−0.01	−0.04	+0.20	−0.08	+0.20	−0.05
$[5H(2,6\text{-Py})]^{2+}$ HS	+1.02	+1.02	−0.12	−0.12	+0.21	+0.21	+0.07	−0.06	+0.10	−0.05	+0.10	−0.06
$[5H(2,6\text{-Py})]^{2+}$ BS	+1.08	−1.02	−0.12	+0.12	+0.21	−0.21	−0.03	−0.00	−0.05	+0.02	−0.05	+0.04
$[5H(3,5\text{-Py})]^{+}_{s}$	+0.33	+0.32	−0.00	+0.00	+0.12	+0.12	−0.06	+0.20	−0.05	−0.01	−0.04	+0.20
$[5H(3,5\text{-Py})]^{+}_{as}$	+0.78	+0.01	−0.05	−0.01	+0.21	+0.02	−0.05	+0.13	−0.04	+0.03	−0.04	+0.14
$[5H(3,5\text{-Py})]^{2+}$ HS	+1.01	+1.01	−0.13	−0.13	+0.21	+0.21	−0.05	+0.11	−0.07	+0.10	−0.07	+0.11
$[5H(3,5\text{-Py})]^{2+}$ BS	+1.02	−1.02	−0.11	+0.11	+0.20	−0.20	+0.00	−0.00	−0.02	+0.00	+0.02	+0.00
$[5H(1,3\text{-Ph})]^{+}_{s}$	+0.30	+0.30	+0.01	+0.01	+0.11	+0.11	−0.04	−0.01	−0.04	+0.21	−0.08	+0.21
$[5H(1,3\text{-Ph})]^{+}_{as1}$	+0.72	+0.01	−0.03	−0.01	+0.21	+0.02	−0.03	+0.04	−0.04	+0.16	−0.06	+0.13
$[5H(1,3\text{-Ph})]^{2+}$ HS	+0.98	+0.98	−0.12	−0.12	+0.22	+0.22	−0.07	+0.12	−0.07	+0.12	−0.06	+0.12
$[5H(1,3\text{-Ph})]^{2+}$ BS	+0.99	−0.99	−0.10	+0.10	+0.20	−0.21	−0.02	−0.00	+0.02	+0.01	+0.00	−0.01

[a] X(1) = N(1) for $[5H(2,6\text{-Py})]^{n+}$ and $[5H(3,5\text{-Py})]^{n+}$; X(1) = C(γ) for $[5H(1,3\text{-Ph})]^{n+}$ (see Scheme 1 for atom labeling).

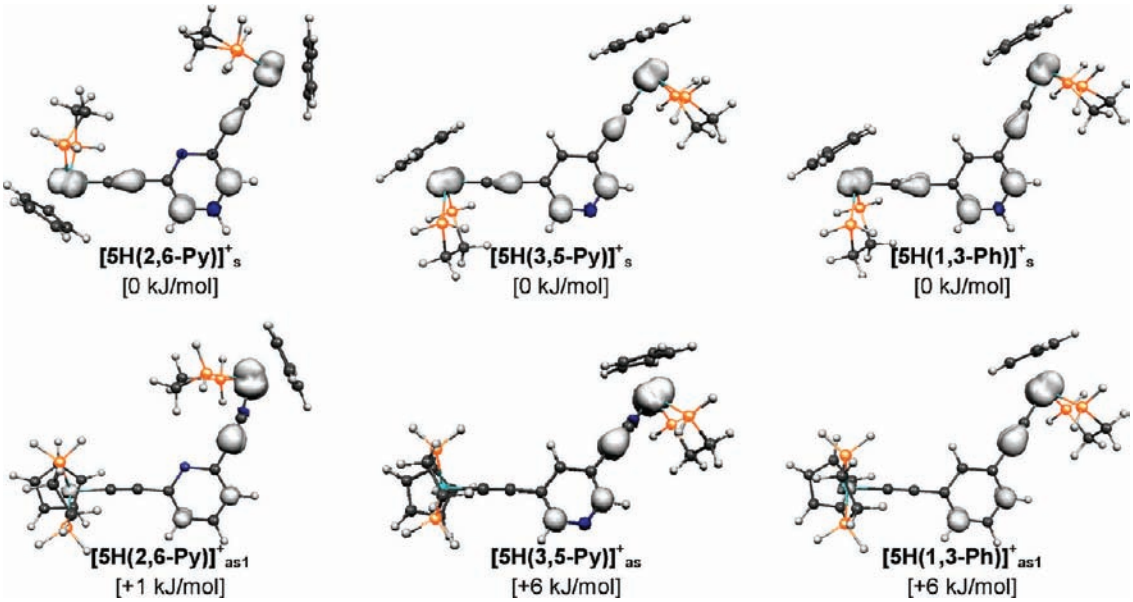

Figure 3. Comparison of the spatial distribution of spin densities computed for symmetrical and asymmetrical cationic model compounds for $[5H(2,6\text{-Py})]^{+}$, $[5H(3,5\text{-Py})]^{+}$, and $[5H(1,3\text{-Ph})]^{+}$. Contour values are ±0.004 e/bohr^3.

0.72 e for $[5H(2,6\text{-Py})]^{+}_{as1}$, $[5H(3,5\text{-Py})]^{+}_{as}$, and $[5H(1,3\text{-Ph})]^{+}_{as1}$, respectively). This Fe atom can then be considered to be formally Fe^{III}, and the other one can be formally considered to be Fe^{II}. This is in agreement with the computed Fe−C(α) distances (vide supra).

Part of the unpaired electron is also localized on C(β) of the ethynyl groups and along the long branch of either the pyridyl or the phenyl groups, regardless of the valence-delocalized or valence-trapped geometries (see Figure 3). Delocalization of the unpaired electron in these mixed-valence species implies some electronic communication between the two metals. Indeed, the unpaired electron is statistically more than 30% located on the long branch of the aromatic ring. Thus, it seems that the pathway for such a connection in these molecular models involves the long branch of the aromatic ring.

It is known that DFT often overestimates charge delocalization in mixed-valence systems.[24−26] We performed complete active space self-consistent field (CAS-SCF) computations, together with internally contracted multireference configuration interaction (MR-CI) (see the Computational Details section) in order to propose a reasonable benchmarking of DFT computations and to take into account the effects of the multireference nature of the systems. The main results are collected in Table 4. From the spectrum analysis, one can see that, in all of the cases, the trapped Class II mixed-valence state is energetically preferred. It turns out that the electronic structure of the systems is much more complicated than the one expected from the simple two-state model of Marcus theory, as is the case for some other different MV systems.[37] Indeed, a quite complicated manifold of six low-energy states for the asymmetrical geometries and six more for the symmetrical conformations arises. It is highly probable that more than one state can participate in the charge-transfer mechanism. The charge localization is also confirmed by the analysis of the x-component of the dipole moment that is the one almost parallel to the Fe···Fe axis. In the asymmetric conformations the dipole moment component is quite large and the sign changes between the states, indicating localization on the left or the right metal atoms, respectively. On the other hand, in the case of the symmetrical geometries, the value of the dipole moment is quite small, indicating a symmetrical

dx.doi.org/10.1021/ic2016148 | Inorg. Chem. 2011, 50, 12601−12622

Table 4. CAS-SCF and MR-CI Low Energy Spectrum (E, eV) and Dipole Moments (μ, a.u.) of the Symmetrical $[5H(2,6\text{-Py})]^+_s$, $[5H(3,5\text{-Py})]^+_s$, $[5H(1,3\text{-Ph})]^+_s$ and Asymmetrical, $[5H(2,6\text{-Py})]^+_{as1}$, $[5H(3,5\text{-Py})]^+_{as}$, $[5H(1,3\text{-Ph})]^+_{as1}$ Complexes

CAS-SCF				MR-CI			
$[5H(2,6\text{-Py})]^+_{as1}$		$[5H(2,6\text{-Py})]^+_s$		$[5H(2,6\text{-Py})]^+_{as1}$		$[5H(2,6\text{-Py})]^+_s$	
E (eV)	μ (a.u.)	E (eV)	μ (a.u.)	E (eV)	μ (a.u.)	E (eV)	μ (a.u.)
0.0000	−6.79	0.4779	−1.62	0.0000	−6.10	0.3554	0.28
0.3052	−6.91	0.4797	1.63	0.3097	−6.21	0.3510	−0.28
0.6034	11.40	0.7638	−0.13	0.6014	10.69	0.6541	0.01
0.8126	11.53	0.7711	0.13	0.8484	10.82	0.6610	−0.01
0.9493	−6.79	1.4753	0.03	0.9789	−6.12	1.3500	0.03
1.5414	11.43	1.4961	−0.03	1.5654	10.73	1.3726	−0.03
$[5H(3,5\text{-Py})]^+_s$		$[5H(3,5\text{-Py})]^+_{as}$		$[5H(3,5\text{-Py})]^+_s$		$[5H(3,5\text{-Py})]^+_{as}$	
E (eV)	μ (a.u.)	E (eV)	μ (a.u.)	E (eV)	μ (a.u.)	E (eV)	μ (a.u.)
0.2476	8.06	0.1692	1.32	0.2245	7.34	0.1119	0.66
0.3267	−11.39	0.4451	−1.99	0.3209	−10.73	0.3936	−2.07
0.4569	8.21	0.4500	1.99	0.4690	7.47	0.3981	2.07
0.9979	−11.32	1.1520	−0.68	0.9959	−10.66	1.0915	−0.62
1.1835	8.12	1.1672	0.69	1.1872	7.39	1.1078	0.62
$[5H(1,3\text{-Ph})]^+_{as1}$		$[5H(1,3\text{-Ph})]^+_s$		$[5H(1,3\text{-Py})]^+_{as1}$		$[5H(1,3\text{-Ph})]^+_s$	
E (eV)	μ (a.u.)	E (eV)	μ (a.u.)	E (eV)	μ (a.u.)	E (eV)	μ (a.u.)
0.2202	8.44	0.1524	−0.03	0.2007	7.76	0.1533	−0.04
0.3311	−10.78	0.4314	0.02	0.3304	−10.18	0.4446	0.12
0.4287	8.58	0.4372	−0.02	0.4433	7.89	0.4499	−0.12
1.0069	−10.73	1.1424	0.01	1.0046	−10.11	1.1421	0.02
1.1594	8.48	1.1602	−0.01	1.1670	7.80	1.1614	−0.02

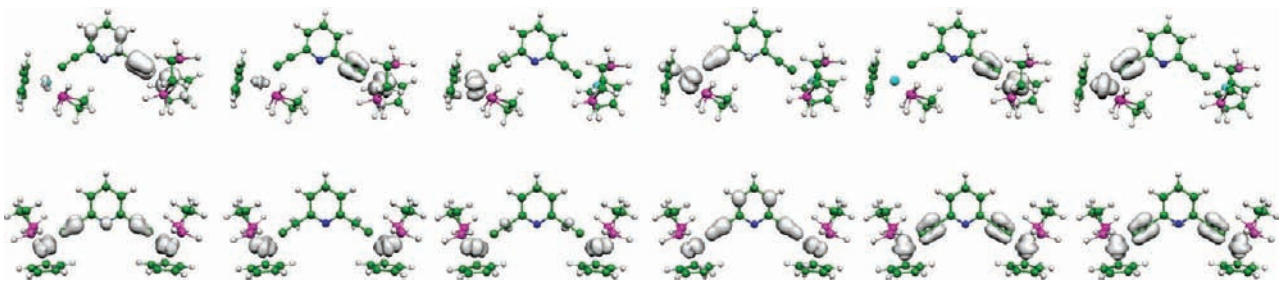

Figure 4. Spatial distribution of the computed CAS-SCF spin density for the six first states of $[5H(2,6\text{-Py})]^+_{as1}$ (top) and $[5H(2,6\text{-Py})]^+_s$ (bottom). Contour values are 0.001 e/bohr^3.

distribution of the charge and, therefore, an equitable partition of the hole between the two Fe centers.

As far as the effect of the dynamic correlation is concerned, one can see that, as expected, the MR-CI results in a diminishing of the spin localization, giving rise to smaller dipole moments and energy differences between localized and delocalized states than CAS-SCF. Nevertheless, the general trend is not altered and the localization of the charge appears stronger than within the DFT calculations.

It is also interesting to note that the $[5H(2,6\text{-Py})]^+$ complex behaves quite differently from the other two. Indeed, in that case, the first nonsymmetrical excited state has a lower energy than the symmetrical ground state, and, moreover, from the dipole analysis, it appears that the first nonsymmetrical excited state has the charge localized on the same Fe atom as in the nonsymmetrical ground state. This could suggest the possibility of the presence of equilibrium between two charged-trapped conformers, as apparently experimentally confirmed for $[5(2,6\text{-Py})]^+$ by vibrational spectroscopy (see below). Actually, in order to confirm this aspect, one first should perform an excited-state geometry optimization at CAS-SCF level; however, because of the computational cost, this aspect would be far beyond the objective of the present work.

The CAS-SCF spin density for the six nonsymmetrical and symmetrical states is given in Figure 4 for $[5H(2,6\text{-Py})]^+$ only. The localization of the nonsymmetrical structures is confirmed, as well as the relationship with the sign of the dipole moment. The weaker delocalization on the bridging unit, with respect to the DFT results, is also confirmed. Coherently with DFT results, the role of the ethynylaryl bridge appears crucial in defining the path of the charge transfer, and, quite interestingly, its importance seems to be quite different in the ground and excited states.

A somewhat different DFT spin distribution is found for the HS dicationic systems $[5H(2,6\text{-Py})]^{2+}$, $[5H(3,5\text{-Py})]^{2+}$, and $[5H(1,3\text{-Ph})]^{2+}$. As expected, important spin density is localized on both Fe centers, but substantial density is also found on the ethynyl groups and the entire central ring this time (see Table 3). Note that the spin population on the Fe centers in the pyridinyl-containing compounds $[5H(2,6\text{-Py})]^{2+}$ and $[5H(3,5\text{-Py})]^{2+}$ is slightly larger than the corresponding spin population in $[5H(1,3\text{-Ph})]^{2+}$ (1.02 and 1.01 vs 0.98).

dx.doi.org/10.1021/ic2016148 | Inorg. Chem. 2011, 50, 12601−12622

Scheme 3. Reaction of an Iron Halide with 2,6-Bis(trimethylsilylethynyl)pyridine or 3,5-Bis(trimethylsilylethynyl)pyridine in Methanol To Produce Target Complexes 5(2,6-Py) and 5(3,5-Py)[a]

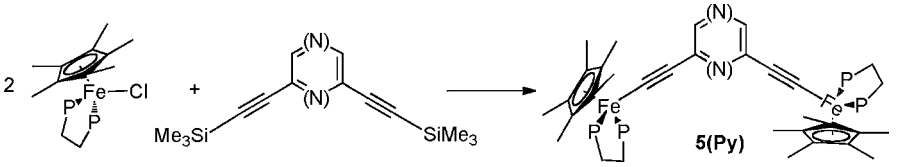

[a]Key reagents: Method A, KPF_6, KF, $KOBu^t$; Method B, $NaBPh_4$, K_2CO_3, $KOBu^t$.

This might account for smaller J values computed for the former (see above). Thus, our results indicate that the entire bridge is involved in the magnetic coupling between the two magnetic centers in all cases and that the N atom is expected to reduce the magnetic interaction if its geometry can freely relax ("unrelaxed" conformers may be trapped in the solid state), regardless of its position in the ring.

WHAT DO EXPERIMENTS SHOW?

1. Synthesis of 5(2,6-Py) and 5(3,5-Py). Reaction of the iron halide Cp*(dppe)FeCl with 0.5 equiv of 2,6-bis(trimethylsilylethynyl)pyridine or 3,5-bis(trimethylsilylethynyl)pyridine in methanol and in the presence of $NaBPh_4$ or KPF_6 and KF or K_2CO_3 to promote the cleavage of the trimethylsilyl group provided the target complexes **5(2,6-Py)** and **5(3,5-Py)** in good yield (79%–98%) after a final treatment with a strong base (Scheme 3). As extensively described, large counteranions such as PF_6^- and BPh_4^- favor the heterolytic metal–halogen bond dissociation in polar solvent.[38,39] In the case of the synthesis of the closely related complex **5(1,3-Ph)**, it was found that the cleavage of the trimethylsilyl group under such conditions is associated with the formation of a stoichiometric amount of KOMe.[38] This base was able to deprotonate the bis(vinylidene) formed as a reaction intermediate. In the case of the **5(2,6-Py)** and **5(3,5-Py)** complexes, treatment with an excess of a strong base such as $KOBu^t$ was needed. Possibly, the pyridine group electronically enriched by the organometallic fragments is basic enough to retain a proton in the experimental conditions. Indeed, the IR spectra of the crude products analyzed before treatment with $KOBu^t$ displayed an additional IR band at 1992 cm^{-1}, which does not belong to the neutral complexes. The more-basic character of the pyridine ligand, with respect to acetylide, has been reported for many years.[40] Extraction of the crude solid residue with toluene or CH_2Cl_2 (see the Experimental Section) and washing of the resulting material with pentane allowed the isolation of the target neutral complexes as pure orange thermally stable powders.

The analytically pure solid complexes **5(2,6-Py)** and **5(3,5-Py)** were characterized by IR and multinuclear NMR spectroscopies, ^{57}Fe Mössbauer spectrometry, and X-ray data which confirmed the proposed structures. Specifically, the IR spectra (recorded in CH_2Cl_2) display a typical absorption band for the C≡C triple bond at 2043 and 2044 cm^{-1} for **5(2,6-Py)** and **5(3,5-Py)**, respectively. The frequencies of these bands are slightly lower than the frequency found for the **5(1,3-Ph)** complex, which appears at 2049 cm^{-1}. This small shift probably reflects the increasing electron-withdrawing character of the aromatic ring when a CH group is replaced by nitrogen. Infrared absorptions characteristic of the pyridyl unit are also observed at 1558, 1548, and 1538 cm^{-1} for **5(2,6-Py)** and 1586 and 1555 cm^{-1} for **5(3,5-Py)** (Nujol).

The better solubility of **5(2,6-Py)** and **5(3,5-Py)**, with respect to **5(1,3-Ph)**, allowed observation of the ^{13}C resonances of the ethynyl fragments in the ^{13}C NMR spectra at δ 138.7 (Cα, $^2J_{CP}$ = 39 Hz), 123.1 (Cβ), and δ 140.7 (Cα, $^2J_{CP}$ = 39 Hz), 117.3 (Cβ), respectively. The ^{31}P NMR spectra of **5(2,6-Py)** and **5(3,5-Py)** exhibit a single and sharp resonance at δ 102.1 and 101.6, respectively.

2. Molecular Structure of 5(2,6-Py) and 5(3,5-Py). To provide insight into the mutual arrangement of the organometallic building blocks and their orientation, with respect to the connecting heterocycle, X-ray molecular structures of **5(2,6-Py)** and **5(3,5-Py)** were determined. Crystals of **5(2,6-Py)** were grown by slow diffusion of pentane into a dichloromethane solution of the complex, whereas crystals of **5(3,5-Py)** were obtained by slow diffusion of hexane into a toluene solution of the complex. The unit cells of **5(2,6-Py)** and **5(3,5-Py)** contain 4 and 2 molecules, respectively. The molecular structures are shown in Figure 5, and the X-ray data collection conditions are summarized in the Experimental Section, while the crystal data, including selected structure refinement parameters, are given in Table 5. The complex **5(2,6-Py)** crystallizes in the monoclinic space group $P2_1/c$. Its meta analogue, **5(3,5-Py)**, crystallizes in the triclinic space group $P\bar{1}$. For the latter compound, the unit cell contains 1.5 molecules of hexane, one of these solvates being strongly disordered and difficult to model.

As invariably observed for all the members of the Cp*(dppe)Fe family of complexes, the two metal moieties adopt pseudo-octahedral geometries with bond lengths and angles in previously established ranges.[2,41] Pertinent bond lengths are given in Table 1. They compare rather well with the corresponding DFT-computed values, with deviations of <0.02 Å within the metal–carbon chain.

As apparent from the ORTEP diagrams (Figure 5), the Fe-Cp* centroids of the two Cp*(dppe)Fe are roughly coplanar with the plane of the pyridyl alkynyl linker in **5(2,6-Py)**, whereas they are more or less oriented in "anti" positions relative to it in **5(3,5-Py)**. For both complexes, the torsion angles between these Fe–Cp* vertexes are nevertheless closer to 90° than to 180° (Cp*1–Fe1–Fe2–Cp*2 = 92° ± 1° and 115°, respectively). Most likely, these different conformations, resulting in the dominant interaction of different (orthogonal) symmetry-based combinations of d_{Fe} orbital sets with the bridge π-manifold for each complex are induced by packing forces rather than by (intra)molecular interactions. While the intramolecular through-bond Fe–Fe mean distance is similar for both isomers (ca. 11.7 Å), the through-space intramolecular Fe–Fe distance is significantly shorter, but slightly longer in the case of **5(3,5-Py)** (9.7 Å vs 10.1 Å).

3. Cyclic Voltammetry of 5(2,6-Py) and 5(3,5-Py). The initial scans in the cyclic voltammograms of **5(2,6-Py)** and **5(3,5-Py)** recorded from −1 V to +1 V (vs standard calomel electrode, SCE) show two chemically reversible oxidation waves separated by 0.16 and 0.11 V, respectively. In both series,

dx.doi.org/10.1021/ic2016148 | Inorg. Chem. 2011, 50, 12601–12622

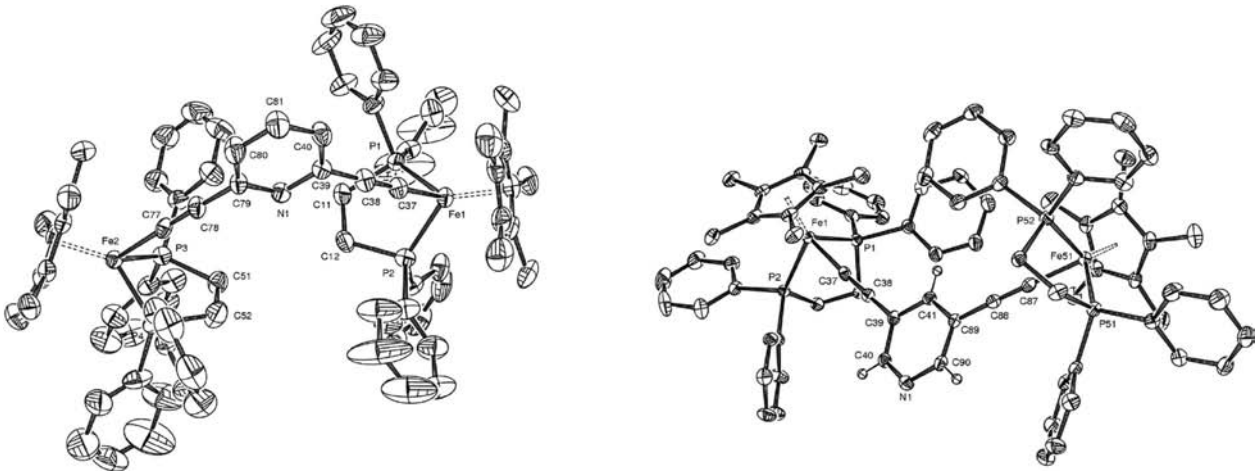

Figure 5. Molecular structures of **5(2,6-Py)** (left) and **5(3,5-Py)**·$^3/_2C_6H_{12}$ (right), showing thermal ellipsoids at the 50% probability level. Hydrogen atoms and solvent molecules have been removed for the sake of clarity.

Table 5. Crystal Data, Data Collection, and Refinement Parameters for 5(2,6-Py) and 5(3,5-Py)

	5(2,6-Py)	5(3,5-Py)
formula	$C_{162}H_{162}Fe_4N_2P_8$	$C_{81}H_{81}Fe_2N_1P_4 \cdot {}^3/_2C_6H_{12}$
fw	2608.10	1431.29
cryst syst	monoclinic	triclinic
space group	$P2_1/c$	$P\bar{1}$
a (Å)	22.6272(6)	9.3407(4)
b (Å)	19.8317(4)	18.4949(8)
c (Å)	31.1009(7)	24.4587(8)
α (deg)	90.0	67.320(3)
β (deg)	95.4350(10)	79.629(3)
γ (deg)	90.0	84.274(3)
V (Å^3)	13893.3(6)	3832.8(3)
Z	4	2
density, $D_{(calcd)}$ (g cm^{-3})	1.247	1.240
crystal size (mm)	0.3 × 0.3 × 0.22	0.15 × 0.08 × 0.08
F(000)	5488	1518
abs coef (mm^{-1})	0.554	0.508
No. total refl/No. unique refl	66511/26421	27524/15897
No. of variables/ No. refl > 2σ(I)	1585/12894	852/15897
final R	0.0594	0.0544
R_w	0.1350	0.1653
goodness of fit/F^2 (S_w)	1.005	1.034

these redox processes correspond to the formation of the MV species Fe^{II}–Fe^{III} and homovalent Fe^{III}–Fe^{III} derivatives at the platinum electrode (see Table 6).

Table 6. Electrochemical Data for Selected Complexes[a]

compd	$E_1^0(\Delta E_p)$	$E_2^0(\Delta E_p)$	ΔE^0	K_c (25 °C)	ref
2a	−0.27(0.06)	−0.01(0.06)	0.26	2.5 × 10^4	42
5(1,3-Ph)	−0.23(0.08)	−0.10(0.09)	0.13	1.3 × 10^2	38
5(2,6-Py)	−0.18(0.08)	−0.02(0.08)	0.16	4.8 × 10^2	this work
5(3,5-Py)	−0.14(0.07)	−0.03(0.07)	0.11	0.9 × 10^2	this work
8(Ph)	−0.15(0.08)				43
8(2-Py)	−0.08(0.09)				44
8(3-Py)	−0.11(0.09)				44

[a] In CH_2Cl_2, 0.1 M tetra-*n*-butylammonium hexafluorophosphate, scan rate = 0.1 V/s, Pt electrodes, V vs SCE.

As expected, the substitution of a CH group by the more-electronegative N atom in the connecting aromatic cycle makes the two one-electron oxidations of these complexes more difficult, in full agreement with DFT calculations (see above). Indeed, complexes **5(2,6-Py)** and **5(3,5-Py)** are oxidized at a less-negative potential than **5(1,3-Ph)**, by 0.05 and 0.09 V, respectively. This is supported by the theoretical calculations which show that introducing a N atom in the central ring leads to greater ionization potentials, because of larger electrostatic stabilization (5.45 and 5.48 eV for **5H(2,6-Py)** and **5H(3,5-Py)**, and 5.34 eV for **5(1,3-Ph)** (vide supra). It is also interesting to note that, for the related mononuclear complexes, oxidation of **8(Ph)** is easier than that of **8(2-Py)** and **8(3-Py)**, but the effect of the nitrogen on the redox potential of the Fe building block is larger when the alkynyl group is linked to the ring on the *ortho* position than in the *meta* position, with respect to the heteroatom. Such a different behavior between the mononuclear and binuclear series suggests that the electronic interaction between the two metal centers plays an important role. To this respect, one can note that the effect of the N atom on the redox waves is dependent on its position in the aromatic ring. With respect to the reference compound **5(1,3-Ph)**, introduction of the nitrogen in the short through-bond path increases the value of ΔE^0 by 0.03 V, whereas its presence on the long path decreases the value of ΔE^0 by 0.02 V (see Table 6).

The equilibrium constant for the comproportionation reaction (eq 1) where −*B*− represents the bridge between the metal atoms, ranges from 480 for **5(2,6-Py)** to 100 for **5(3,5-Py)**, according to eq 2:

$$\{[M^{red}] - B - [M^{red}]\}^{n+} + \{[M^{ox}] - B - [M^{ox}]\}^{(n+2)+} \overset{K_C}{\rightleftharpoons} 2\{[M^{red}] - B - [M^{ox}]\}^{(n+1)+} \quad (1)$$

$$\Delta E = E_2 - E_1 = -\left(\frac{RT}{F}\right) \log K_C \quad (2)$$

The knowledge of K_C allows for determination of the molar fractions of the species present in solution. In particular, when 1 equiv of the neutral complex reacts with 1 equiv of one-electron oxidized reagent, the molar fractions of the MV species at 293 K are ~0.92 and ~0.82 for **5(2,6-Py)** and **5(3,5-Py)**, respectively.

dx.doi.org/10.1021/ic2016148 | Inorg. Chem. 2011, 50, 12601–12622

Table 7. ^{57}Fe Mössbauer Parameters for $[5(2,6\text{-Py})][PF_6]_n$, $[5(3,5\text{-Py})][PF_6]_n$ and $[5(1,3\text{-Ph})][PF_6]_n$ (n = 0, 1, 2) at 80 K[a]

	IS[a] (QS) Γ (mm s^{-1})			
compd	n = 0	n = 1	n = 2	ref
$[5(2,6\text{-Py})][PF_6]_n$	0.254 (1.991) 0.114	0.250 (1.936) 0.130 0.253 (0.881) 0.175	0.253 (0.886) 0.163	this work
$[5(3,5\text{-Py})][PF_6]_n$	0.260 (2.042) 0.126	0.230 (1.864) 0.137 0.241 (0.815) 0.157	0.254 (0.889) 0.153	this work
$[5(1,3\text{-Ph})][PF_6]_n$	0.20 (2.00)	0.25 (2.00) 0.25 (0.85)	0.28 (0.89)	9
$[8(2\text{-Py})][PF_6]_n$	0.243 (1.870) 0.119	0.232 (0.917) 0.146		49
$[8(3\text{-Py})][PF_6]_n$	0.255 (2.036) 0.117	0.249 (0.869) 0.162		49

[a]The velocity is referenced to iron metal.

4. Preparation and Isolation of the Oxidized Species. Based on the full reversibility of the CV waves (i^a_p/i^c_p = 1), the doubly oxidized complexes $[5(2,6\text{-Py})][PF_6]_2$ and $[5(3,5\text{-Py})][PF_6]_2$ were considered as accessible synthetic targets. According to a well-established procedure, the neutral parents were reacted with 1.95 equiv of $[(C_5H_5)_2Fe][PF_6]$ in THF. The complexes $[5(2,6\text{-Py})][PF_6]_2$ and $[5(3,5\text{-Py})][PF_6]_2$ were precipitated from the THF solution via the addition of pentane. The MV complexes $[5(2,6\text{-Py})][PF_6]$ and $[5(3,5\text{-Py})][PF_6]$ were obtained from the comproportionation reaction between the homovalent complexes (n = 0 and n = 2) in the 1:1 ratio and isolated by removal of the solvent under vacuum, or in situ generated via the same way. All these new paramagnetic species were characterized by CVs identical to the parent neutral complexes, as well as Mössbauer, EPR, FTIR, NIR and UV−vis spectroscopies. As a powder, these compounds are thermally stable for several weeks. In contrast with the reference compounds $5(1,3\text{-Ph})[PF_6]_n$, these new paramagnetic complexes are not very stable in solution. They slowly decompose in THF and much more quickly in CH_2Cl_2. The spectroscopic measurements were repeated at least three times with freshly and independently prepared solutions, and the molar extinction coefficients were calculated using K_C to determine the real concentration of all the species present in solution.

5. ^{57}Fe Mössbauer Spectrometry. The Mössbauer spectra of the six compounds $[5(2,6\text{-Py})][PF_6]_n$ and $[5(3,5\text{-Py})][PF_6]_n$ (n = 0, 1, 2) were run at zero field (80 K) and least-squares fitted with Lorentzian line shapes.[45] The isomer shift (IS), quadrupole splitting (QS), and half-width at half-height (Γ) are collected in Table 7. The spectra of the bis-iron(II) neutral complexes exhibit a single doublet with IS and QS parameters in line with previous observations of compounds of the same series.[2,46,47]

In the case of the bis-iron(III) dicationic complexes $[5(2,6\text{-Py})][PF_6]_2$ and $[5(3,5\text{-Py})][PF_6]_2$, the parameters are characteristic of Fe^{III} centers and compare well with data found for other bis-iron(III) dications and monoiron(III) relatives.[2,46,48] The IS and QS parameters are very similar for both compounds and $[5(1,3\text{-Ph})][PF_6]_2$, indicating that replacement of a CH group by N in the aromatic ring slightly modifies the electronic density of the iron nuclei and its bonding with the connected atoms.[46] This is indeed what is found theoretically for the **5H** series. Moreover, these spectra confirm that the isolated Fe^{III} complexes are thermally stable in the solid state, free of impurities and establish their low spin d^5 character. The data obtained for the neutral and dicationic binuclear complexes compare well with those found for the mononuclear model compounds $[8(2\text{-Py})][PF_6]_n$ and $[8(3\text{-Py})][PF_6]_n$ (n = 0, 1).[49]

^{57}Fe Mössbauer spectroscopy is a powerful means for studying MV species in the solid state.[50,51] Indeed, direct observation of iron nuclei allows the determination of the oxidation states of the metals and gives an estimation of the distribution between the remote ends and the organic bridge. Moreover, it provides the evaluation of the electron-transfer rate between the redox-active centers relative to the acquisition time of the technique. The presence of two distinct doublets in the spectrum is diagnostic of a localized valence with a rate constant $k_e < 10^{-6}$ s^{-1}, whereas observation of a single averaged doublet is characteristic of detrapped valence with $k_e > 10^{-9}$ s^{-1}.[22,52] The ^{57}Fe Mössbauer spectra of the MV complexes $[5(2,6\text{-Py})][PF_6]$ and $[5(3,5\text{-Py})][PF_6]$ display two well-separated doublets with relative spectral absorption areas in 1:1 ratio, diagnostic of localized valence. It is noteworthy that, within the accuracy of the fits of the experimental spectra, an increase of the line broadening cannot be detected for the MV complexes, with respect to those of the homovalent parent derivatives. Consequently, the exchange rate constants k_e for the intramolecular electron transfer are clearly below 10^{-6} s^{-1}. As similar observations were previously reported for the MV complex $[5(1,3\text{-Ph})][PF_6]$, it can be concluded that substitution of a C−H fragment by a N atom in the aromatic ring of these MV complexes do not have a detectable effect on the intramolecular electron transfer (ET) rate for samples in the solid state.

In the case of $[5(2,6\text{-Py})][PF_6]$, the spectral parameters of the Fe^{II} and Fe^{III} centers are exactly the same as those found for the homovalent parents, indicating that the spin density is essentially localized on one metal site. For the MV $[5(3,5\text{-Py})][PF_6]$, one can note that the IS values found for both Fe sites are smaller than the corresponding data found for the homovalent Fe^{II}Fe^{II} and Fe^{III}Fe^{III} complexes, suggesting that the bridging ligand might play a minor role in the distribution of the spin density. These observations match well with the DFT data obtained for the localized spin isomers. In addition, the small QS parameter found for the Fe^{II} center of this MV complex suggests that the weight of the valence bond mesomers **B** and **C** (Scheme 4) is not negligible in the description of the electronic structure of this MV complex. Note that similar conclusions have already been drawn for the mononuclear complex $[8(3\text{-Py})][PF_6]$.[49]

6. Glass EPR Spectroscopy and Solid-State Magnetic Susceptibility. The sample of the MV compounds $[5(2,6\text{-Py})][PF_6]$ and $[5(3,5\text{-Py})][PF_6]$ were prepared by reacting the corresponding neutral complexes with 0.3−0.4 equiv of

dx.doi.org/10.1021/ic2016148 | Inorg. Chem. 2011, 50, 12601−12622

Scheme 4. Selected Possible Mesomeric Structures for [5(3,5-Py)][PF$_6$]

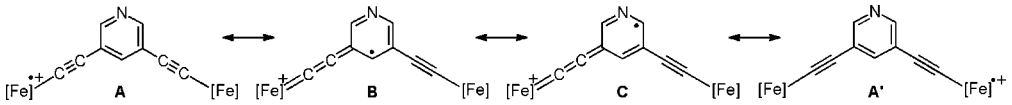

$[(C_5H_5)_2Fe][PF_6]$ in order to obtain samples that are free of the dicationic species. The X-band EPR spectra were run at 77 K in a rigid glass ($CH_2Cl_2/C_2H_4Cl_2$, 1:1) for **[5(2,6-Py)][PF$_6$]$_n$** and **[5(3,5-Py)][PF$_6$]$_n$** (n = 1, 2). The spectra of the monocationic species display three features corresponding to the three components of the g-tensor, as expected for d^5 low-spin iron(III) in a pseudo-octahedral environment. The g-values extracted from the spectra are collected in Table 8.

Table 8. EPR Data for [5(2,6-Py)][PF$_6$]$_n$, [5(3,5-Py)][PF$_6$]$_n$, and [5(1,3-Ph)][PF$_6$]$_n$ (n = 1, 2)

compd	g_1	g_2	g_3	g_{iso} [a]	Δg [b]	ref
[5(2,6-Py)][PF$_6$]	1.972	2.028	2.482	2.161	0.510	this work
[5(3,5-Py)][PF$_6$]	1.971	2.029	2.497	2.166	0.526	this work
[5(1,3-Ph)][PF$_6$]	1.975	2.032	2.505	2.170	0.530	9
[5(2,6-Py)][PF$_6$]$_2$ [c]	1.968	2.027	2.507	2.167	0.539	this work
[5(3,5-Py)][PF$_6$]$_2$ [c]	1.974	2.029	2.497	2.167	0.523	this work
[5(1,3-Ph)][PF$_6$]$_2$	2.10 (ΔH_{pp} = 550 G)					48
[8(Ph)][PF$_6$]	1.975	2.033	2.464	2.157	0.489	43
[8(2-Py)][PF$_6$]	1.990	2.024	2.500	2.163	0.534	49
[8(3-Py)][PF$_6$]	1.967	2.028	2.490	2.162	0.521	49

[a] $g_{iso} = (g_1 + g_2 + g_3)/3$. [b] $\Delta g = g_3 - g_1$. [c] The spectrum shows an additional feature at g = 2.15 (see text).

The g-values obtained for both MV compounds compare well with those previously obtained for the corresponding mononuclear species **[8(2-Py)][PF$_6$]** and **[8(3-Py)][PF$_6$]**. These data suggest a trapped MV compound with the electronic vacancy strongly localized on a single metal center, in accord with other spectroscopic analyses.

Interestingly, one can note that the tensor of anisotropy (Δg) found for the mononuclear complexes **[8(2-Py)][PF$_6$]** and **[8(3-Py)][PF$_6$]** are significantly larger than the tensor of anisotropy of the reference complex **[8(Ph)][PF$_6$]**, indicating that introduction of the N atom in the aromatic ring reinforces the localization of the spin density on the Fe atoms in agreement with the prediction of DFT calculations. In addition, one can note that this effect is larger when the N atom is located on the small branch between the metal alkynyl fragments. According to DFT calculations, the spin densities on the metal sites are also larger for the MV having a pyridine ring instead of a phenyl cycle in the bridging ligand. As a result, larger Δg-parameters are expected when the connecting arene contains a N atom. In contrast, the Δg-tensors found for the MV complexes **[5(2,6-Py)][PF$_6$]** and **[5(3,5-Py)][PF$_6$]** are smaller than the Δg-tensor obtained for the reference complex **[5(1,3-Ph)][PF$_6$]**. Such an opposite behavior between the mononuclear and the MV series suggests that the intramolecular electron exchange can be faster in the nitrogen-containing compounds. Indeed, for MV compounds of a homogeneous series, it has been suggested that the anisotropy tensor (Δg) decreases as the rate of the intramolecular electron transfer (ET) increases.[51,53] Such a behavior has previously been observed in several cases of the Cp*(dppe)Fe series.[2,3,9] Following the variations of Δg, one can expect that the electron-transfer rates increases very slightly when the N atom is introduced in the long branch of the bridge and more efficiently when nitrogen is located in the short branch.

Solutions of the dicationic complexes prepared either from isolated compounds or by in situ treatment of the neutral complexes with 2 equiv of $[(C_5H_5)_2Fe][PF_6]$ provided spectra with the same tensorial signature with one extra feature located at g = 2.15 for both **[5(2,6-Py)][PF$_6$]$_2$** and **[5(3,5-Py)][PF$_6$]$_2$** complexes. In contrast with previous observations with binuclear $Fe^{III}Fe^{III}$ complexes of the Cp*(dppe)Fe series, the low-temperature EPR spectra of **[5(2,6-Py)][PF$_6$]$_2$** and **[5(3,5-Py)][PF$_6$]$_2$** display well-resolved structure. Indeed, diradicals of this series as **[5(1,3-Ph)][PF$_6$]$_2$**, usually show unresolved broad signals with peak-to-peak separation (ΔH_{pp}) as large as 600 G.[48,54] Similar well-resolved features were obtained for the bis(alkynediyl) complexes [Cp*(dppe)Fe−C≡C(Si-$(CH_3)_2)_x$C≡C−Fe(dppe)Cp*][BPh_4]$_2$ (**6^{2+}**, Chart 1) for which a very weak antiferromagnetic interaction was found between the two iron spin carriers ($J \approx -1$ cm^{-1}).[55] In the case of the bis-iron(III) complexes **[5(2,6-Py)][PF$_6$]$_2$**, **[5(3,5-Py)][PF$_6$]$_2$**, and **[5(1,3-Ph)][PF$_6$]$_2$**, the EPR spectra suggest that the N atom should dramatically modify the relaxation times. Moreover, an additional feature was also observed in the spectra of the dications **[5(2,6-Py)][PF$_6$]$_2$** and **[5(3,5-Py)][PF$_6$]$_2$**, which probably results from the presence in the glassy solution of several conformers with different EPR signatures. Indeed, the triplet stabilization depends strongly on the relative orientations of the Cp*(dppe)Fe moieties, as indicated by the calculations. The DFT study on HS **[5H(2,6-Py)]$^{2+}$** and HS **[5H(3,5-Py)]$^{2+}$** shows that the spin density, which illustrates the magnetic conjugating paths, is found on both branches of the central ring. This allows the conclusion that the magnetic exchange configuration should be similar if the same conformation is considered. Nevertheless, as highlighted earlier, the conformations are most probably constrained in the solid state, leading to different magnetic features.

Solid-state magnetization measurements confirm the dramatic role played by the N atom in the aromatic ring. The temperature dependence of the $\chi_M T$ product of powdered samples of **[5(2,6-Py)][PF$_6$]$_2$** and **[5(3,5-Py)][PF$_6$]$_2$** (χ_M is the molar magnetic susceptibility and T the temperature) is plotted against T in Figure 6.

At room temperature, $\chi_M T$ for **[5(2,6-Py)][PF$_6$]$_2$** is equal to 0.795 cm^3 K mol^{-1} with g_{iso} = 2.155, which is slightly lower than the spin-only value (0.870 cm^3 K mol^{-1}), expected for two uncoupled spins $^1/_2$. Upon cooling, $\chi_M T$ remains quasi-constant down to 50 K, then increases upon cooling further and passes through a maximum at T_{max} = 7 K ($\chi_M T_{max}$ = 0.830 cm^3 K mol^{-1}). The experimental data can be reproduced in considering Heisenberg-type superexchange interaction between the two spins $^1/_2$ localized on iron(III) centers ($H = -J\, S_1 \cdot S_2$) and molecular-field (zJ') to account for intermolecular interactions in the solid state. A slightly modified Bleaney−Bowers equation (eq 3)[56] reproduces the thermal variation of

dx.doi.org/10.1021/ic2016148 | Inorg. Chem. 2011, 50, 12601−12622

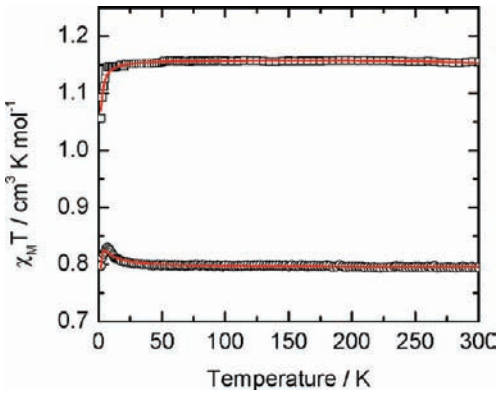

Figure 6. Temperature dependences of $\chi_M T$ for compounds (□) [**5(3,5-Py)**][PF_6]$_2$ and (○) [**5(2,6-Py)**][PF_6]$_2$, with the best-fitted curves (solid lines).

the magnetic susceptibility:

$$\chi_M T = \left(\frac{2N\beta^2}{k}\right) g_{iso}^2 \left[\frac{1}{3 + \exp\left(-\frac{J}{kT}\right) - \frac{2zJ'}{kT}}\right] \quad (3)$$

For the complex [**5(2,6-Py)**][PF_6]$_2$, the best agreement with the experiment was obtained with J = +2.14(5) cm^{-1}, g_{iso} = 2.058(3), and zJ' = −0.55(2) cm^{-1}, clearly establishing that small ferromagnetic interactions propagate through the pyridine ring.

Compound [**5(3,5-Py)**][PF_6]$_2$ is behaving in a completely different manner and gives evidence of the dramatic influence of the heteroatom position in the ring. Indeed, at room temperature, $\chi_M T$ = 1.156 cm^3 K mol^{-1} and remains constant upon cooling down to 8 K. Upon further cooling, $\chi_M T$ decreases slightly to reach 1.06 cm^3 K mol^{-1} at 2 K. The high-temperature dependence attests that, not only the triplet state is the ground state, but this spin state is also the only one populated at room temperature. The temperature dependence of $\chi_M T$ can be reproduced fairly well in considering intermolecular interactions between S = 1 units; i.e., the complex [**5(3,5-Py)**]. To do so, eq 3 is also employed except that J cannot be fitted and must be fixed above 500 cm^{-1}. The best fit was obtained with g_{iso} = 2.153(1) and zJ' = −0.174(5) K. Comparison of the magnetic properties of the new complexes and with the data previously obtained for [**5(1,3-Ph)**][PF_6]$_2$ (J > 300 cm^{-1})[8,57] nicely shows how the substitution of a CH group by a nitrogen atom in the 1,3-bis-(ethynyl)benzene bridge can enhance or reduce the ferromagnetic interaction which occurs between the spin carriers.

A rather large ferromagnetic coupling in the latter is confirmed by the DFT results discussed earlier with a J value of 512 cm^{-1} computed for the model [**5H(1,3-Ph)**]$^{2+}$. On the other hand, experiment and theory differ at first sight for the nitrogen-containing compounds. Theory shows a decrease of J to ca. 90 cm^{-1} for both [**5H(2,6-Py)**]$^{2+}$ and [**5H(3,5-Py)**]$^{2+}$, whereas experiments indicates a decrease of J to ca. 2 cm^{-1} for [**5(2,6-Py)**][PF_6]$_2$ and an enhancement to >500 cm^{-1} for [**5(3,5-Py)**][PF_6]$_2$. We think that the orientation of the metal end-groups in these molecules must be important in governing their magnetic properties. Indeed, in the case of [**5H(3,5-Py)**]$^{2+}$ for instance, the J value increases from 91 cm^{-1} for the ($\perp^2$ $\perp^2$) conformation to 589 cm^{-1} for the ($\perp$ //) conformation, which are close in energy.

7. IR Spectroscopy. The IR spectra of the novel complexes [**5(2,6-Py)**][PF_6]$_n$ and [**5(3,5-Py)**][PF_6]$_n$ (n = 0, 1, 2) were first run with samples in the solid state (KBr; see Figure 7). In accord with the calculated vibrations, the spectra of the neutral compounds present a broad metal-alkynyl stretching band. In the solid state, the bands are broad and, in the case of the complex **5(3,5-Py)**, two maxima are almost resolved. Comparison of these data with those previously reported for **5(1,3-Ph)** indicates that replacement of one CH group by a N atom in the aromatic cycle has almost no effect on the strength of the C≡C triple bond linked to the Fe(II) centers, regardless of its position.[10,11]

Upon double oxidation, the $\nu_{C\equiv C}$ stretches are shifted by 93 cm^{-1} toward the lower frequencies for solid samples of both dicationic complexes [**5(2,6-Py)**][PF_6]$_2$ and [**5(3,5-Py)**]-[PF_6]$_2$. This effect is much larger than that observed for [**5(1,3-Ph)**][PF_6]$_2$ (43 cm^{-1}). Clearly, replacement of a phenyl group by a pyridinyl ring in the bridge of the bis-iron(III) complexes weakens the C≡C triple bonds, regardless of the position of the N atom in the aromatic ring. However, in the case of the mononuclear complexes **8(Ph)**, **8(2-Py)**, and **8(3-Py)**, the lowering of frequencies associated with the one-electron oxidation are rather similar for the three compounds ($\Delta\nu$ = 49, 54, 40 cm^{-1}, respectively).

Interestingly, the IR spectrum of the new MV complex [**5(3,5-Py)**][PF_6] displays two bands located at 1941 and 2042 cm^{-1} with relative intensities close to the 1:2 ratio. One can observe that the energy difference between the frequencies of these bands (101 cm^{-1}) is close to the difference of frequencies found for the $\nu_{C\equiv C}$ of the homovalent Fe^{II}–Fe^{II} and Fe^{III}–Fe^{III} derivatives. These bands can be then safely ascribed to the Fe^{II}–C≡C and Fe^{III}–C≡C stretching modes and constitute the spectroscopic signature of a trapped MV complex. These

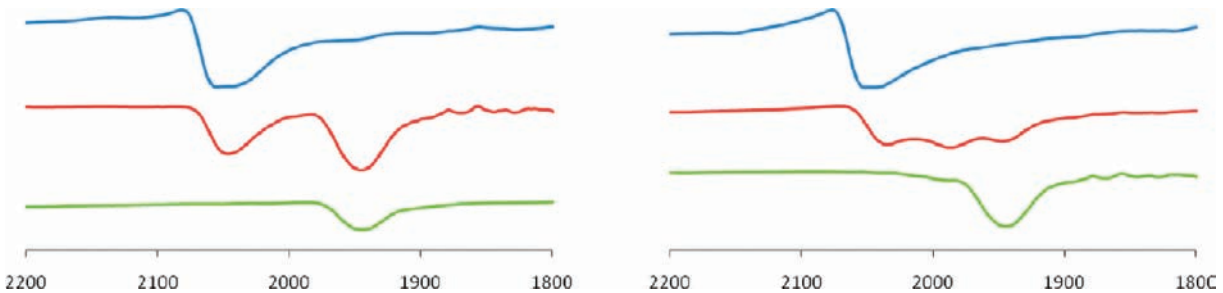

Figure 7. Solid-state IR spectra (KBr, ν cm^{-1}) of [**5(3,5-Py)**][PF_6]$_n$ (left) and [**5(2,6-Py)**][PF_6]$_n$ (right) at 293 K (ν, cm^{-1}; n = 0, top; n = 1, middle; n = 2, bottom).

dx.doi.org/10.1021/ic2016148 | Inorg. Chem. 2011, 50, 12601–12622

data are fully consistent with the calculated spectrum for the trapped MV isomer $[\mathbf{5H(3,5\text{-}Py)}]^{+}_{as}$. Note that very similar IR data were found with the MV complex $[\mathbf{5(1,3\text{-}Ph)}][\mathbf{PF_6}]$.[9]

In contrast, the MV complex $[\mathbf{5(2,6\text{-}Py)}][\mathbf{PF_6}]$ displays a completely different spectrum in the 2100−1800 cm^{-1} range. Measurements on solid samples (KBr) gave spectra with three well-resolved maxima at ν = 1948, 1987, and 2037 cm^{-1} (relative intensities in the ca. 1:1:1 ratio; see Figure 7). Guided by the theory and the simulated IR spectra of the model compound $[\mathbf{5H(2,6\text{-}Py)}][\mathbf{PF_6}]$, the three band stretches were tentatively assigned to the partial overlap of the stretching modes of the two asymmetric isomers $[\mathbf{5(2,6\text{-}Py)}][\mathbf{PF_6}]_{as1}$ and $[\mathbf{5(2,6\text{-}Py)}][\mathbf{PF_6}]_{as2}$, which should differ from one to another mainly by the orientation of the metallic moieties, with respect to the aromatic ring (see above). The possible contribution of a fully symmetric structure is considered to be negligible, based on the Mössbauer and EPR data.

Interconversion between the isomers **as1** and **as2**, which should be similar in energy, can occur upon rotation of the metal end-groups. In the solid state, these rotations around the alkynyl axis are hindered, exchange cannot occur, and the ratio **as1**/**as2** is almost independent of the temperature. This is confirmed by the IR spectrum of $[\mathbf{5(2,6\text{-}Py)}][\mathbf{PF_6}]$ recorded at 4 K (KBr; see Figure 8), which does not differ much from the

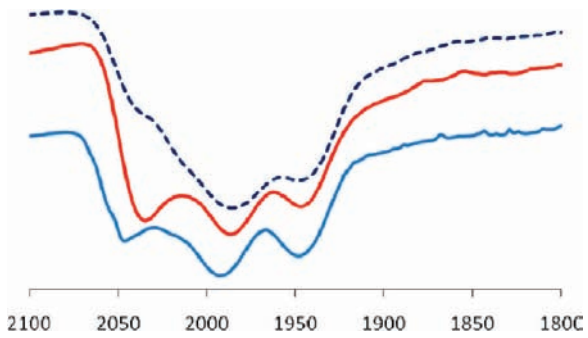

Figure 8. Experimental IR spectra of $[\mathbf{5(2,6\text{-}Py)}][\mathbf{PF_6}]$ (KBr, ν cm^{-1}) for a sample precipitated at 293 K run at 4 K (bottom), 293 K (middle), and precipitated at 193 K run at 293 K (top, dashed line).

spectrum run at 293 K. A small shift of the bond stretches toward higher energies ($\nu_{C\equiv C}$ = 2046, 1993, 1948 cm^{-1}) and a very small decrease of the relative intensity of the band at the highest energy are noted.

Because these isomers should not have exactly the same energies, their thermal population in solution is expected to vary with temperature. For this reason, we compared the IR spectra of solid samples of $[\mathbf{5(2,6\text{-}Py)}][\mathbf{PF_6}]$ obtained by precipitation from a CH_2Cl_2 solution via the addition of pentane performed at 293 and 193 K (see Figure 8). As the spectra found for several samples isolated at 293 K are all similar, the spectrum obtained for the sample prepared at low temperature displays specific features consistent with a different ratio of the two isomers both having two $\nu_{C\equiv C}$ stretches. Apparently, the sample obtained at 193 K contains less of isomer **as1**, which should have two band stretches at distinct energies (close to those found for homovalent $Fe^{II}Fe^{II}$ and $Fe^{III}Fe^{III}$, ca. 2045/1950 cm^{-1}) and more of the less-localized isomer **as2**, the band stretches of which should be ∼1990 and 1950 cm^{-1} (see the Vibrational Spectra section). Consequently, the latter should be slightly more stable.

Assuming that free rotation of the metal termini takes place in solution, interconversion between the $\mathbf{as_1}$ and $\mathbf{as_2}$ isomers should be facile in this case and the ratio $\mathbf{as_1}/\mathbf{as_2}$ should be under thermodynamic control and be dependent on the nature of the solvent and, more particularly, its polarity. The IR spectra of $[\mathbf{5(2,6\text{-}Py)}][\mathbf{PF_6}]$ were recorded in dichloromethane, acetone, and THF. The three spectra display three bands with minima at 1949, 1988, and 2041 cm^{-1} in CH_2Cl_2 and very close frequencies in the other solvents (Figure 9). The

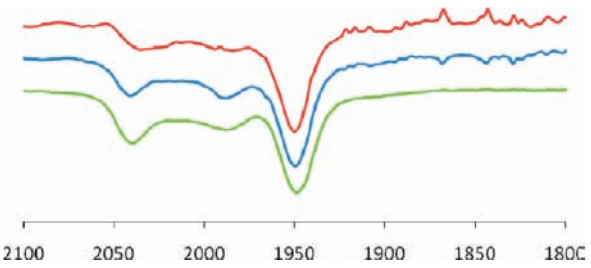

Figure 9. Solution IR spectra of $[\mathbf{5(2,6\text{-}Py)}][\mathbf{PF_6}]$ (ν cm^{-1}) in different solvents (from top to bottom: CH_2Cl_2, acetone, THF).

resolution of the spectra increases with the polarity of the solvents, as well as with the relative intensities of the bands: Close to the 2:1:8 ratio in CH_2Cl_2, it is found to be ∼1:1:6 in acetone.

The rotation rates of the metal building blocks may be dependent on the cation−solvent interactions and have a significant effect on the exchange rate between the isomers. In accord with this assumption, the IR spectrum obtained in CH_2Cl_2 for $[\mathbf{5(2,6\text{-}Py)}][\mathbf{PF_6}]$ presents broad and weakly resolved features, which suggest that the isomers interconvert with an exchange rate at an intermediate regime at the fast IR time scale. In THF and acetone, the $\nu_{C\equiv C}$ bands are well-resolved, suggesting that the exchange rate between the conformers is slower in these solvents.

Comparison of the IR spectra of the mixed-valence compounds $[\mathbf{5(2,6\text{-}Py)}][\mathbf{PF_6}]$, $[\mathbf{5(3,5\text{-}Py)}][\mathbf{PF_6}]$, and $[\mathbf{5(1,3\text{-}Ph)}][\mathbf{PF_6}]$ evidences the role of the N atom, which is dependent on its position in the ring. In the case of the complexes $[\mathbf{5(3,5\text{-}Py)}][\mathbf{PF_6}]$ and $[\mathbf{5(1,3\text{-}Ph)}][\mathbf{PF_6}]$, the experimental FTIR spectra are very similar and fit very well in energy and in intensity with the computed spectra for the asymmetrical ground state. In the case of the MV derivative $[\mathbf{5(2,6\text{-}Py)}][\mathbf{PF_6}]$, substitution of the CH group located on the small branch of the aromatic ring by a N atom produces an important change in the experimental IR spectra, consistent with the presence of at least two geometrical isomers that can interconvert in solution. In agreement with DFT calculations, these isomers should possess different conformations and charge distributions, but both of them must be regarded as trapped MV, based on their Mössbauer and EPR signatures.

8. UV−vis Spectroscopy. The UV−vis spectra of complexes $[\mathbf{5(2,6\text{-}Py)}][\mathbf{PF_6}]_n$ and $[\mathbf{5(3,5\text{-}Py)}][\mathbf{PF_6}]_n$ (n = 0, 1, 2) were recorded at 20 °C in CH_2Cl_2, and the characteristic data are collected in Table 9, along with those found for $[\mathbf{5(1,3\text{-}Ph)}][\mathbf{PF_6}]_n$ (n = 0, 1, 2),[9] for comparison purposes. The spectra of the two neutral complexes are very similar. Beside the intense absorptions at 357 nm that also present shoulders at ∼260 nm, which are assignable to intraligand transitions involving the C_5Me_5, phosphine, and bis(ethynylpyridine) ligands, the electronic absorptions of the

dx.doi.org/10.1021/ic2016148 | Inorg. Chem. 2011, 50, 12601−12622

Table 9. Absorption Data for Complexes $[5(2,6\text{-Py})][PF_6]_n$ and $[5(3,5\text{-Py})][PF_6]_n$ (n = 0, 1, 2) in CH_2Cl_2 at 298 K

compd	absorption λ (nm) (ε ($\times 10^3$ M^{-1} cm^{-1}))
5(2,6-Py)	366 (15), 413 (14), 520 (1), 640 (0.5)
5(3,5-Py)	375 (24), 410 (20),[a] 510 (1.2), 520 (1.2)[a]
5(1,3-Ph)[b]	349 (15.0)[a]
$[5(2,6\text{-Py})][PF_6]$	352 (12),[a] 440 (4),[a] 518 (2.3), 580 (2.2), 680 (2.3)
$[5(3,5\text{-Py})][PF_6]$	380 (9.5),[a] 530 (2.4),[a] 585 (1.8),[a] 670 (1.8)
$[5(1,3\text{-Ph})][PF_6]$[b]	359 (17), 560 (2.6), 650 (4.0)
$[5(2,6\text{-Py})][PF_6]_2$	352 (6.3),[a] 580 (1.5), 680 (1.5)
$[5(3,5\text{-Py})][PF_6]_2$	400 (4),[a] 550 (1),[a] 660 (0.7)[a]
$[5(1,3\text{-Ph})][PF_6]_2$[b]	420 (12), 574 (4.5), 662 (5.5)

[a]Shoulder. [b]From ref 19b.

neutral species also exhibit an intense absorption at the border of the visible range. With reference to related alkynyl iron(II) complexes, this band can be assigned to $d\pi(Fe)\rightarrow\pi^*(C\equiv C)$ metal-to-ligand charge-transfer (MLCT) transitions.[58,59] The position of the N atom hardly affects the transition, but comparison with the absorptions of the complex **5(1,3-Ph)** shows that the presence of nitrogen in the aromatic ring produces a significant red-shift of the transition. The first calculated electronic excitations with a significant oscillator strength reveal that (i) these excited states are described by orbitals lower in energy than the HOMO to unoccupied MOs above the LUMO +4, (ii) they are mainly ligand-to-ligand in character, and (iii) they are different for each rotamer. No clear tendency can be drawn from these TD-DFT calculations between the systems, since only four conformations were computed, whereas, experimentally, all possible conformations can be found in solution.

Spectra of the dications $[5(2,6\text{-Py})][PF_6]_2$ and $[5(3,5\text{-Py})][PF_6]_2$ are also quite similar with three absorption bands in the visible range. By analogy with related compounds, the high-energy band can probably be ascribed to MLCT transitions while the two less-energetic transitions correspond to ligand-to-metal (LMCT) transitions. With reference to $[5(1,3\text{-Ph})][PF_6]_2$, replacement of a CH fragment by N in the aromatic ring of the linker produces only weak shifts of the LMCT transitions.

9. NIR Spectroscopy. The NIR spectra of the neutral complexes **5(2,6-Py)** and **5(3,5-Py)** do not contain any absorption, while the spectra of the doubly oxidized complexes $[5(2,6\text{-Py})][PF_6]_2$ and $[5(3,5\text{-Py})][PF_6]_2$ possess a very weak absorption band (ε < 200 dm^3 mol^{-1} cm^{-1}) centered at ca. 5300 cm^{-1} (see Table 10). Generally observed for all compounds containing the $Cp^*(dppe)Fe^{III}$ fragment, these bands correspond to the forbidden ligand field (LF) transition from the (SOMO-2) to the SOMO.[23]

The experimental spectra of the mono-oxidized complexes $[5(2,6\text{-Py})][PF_6]$ and $[5(3,5\text{-Py})][PF_6]$ were collected from isolated samples of the MV complexes, while the spectrum of the reference complex $[5(1,3\text{-Ph})][PF_6]$ was obtained using spectroelectrochemistry methods (OTTLE cell).[59] The spectra shown in Figure 10 present absorptions of weak intensities with complex shapes. Deconvolution using Gaussian functions revealed the presence of at least three overlapping transitions attributable to the MV species (Table 10).[60] The small component found at ~5300−5400 cm^{-1} for both $[5(2,6\text{-Py})][PF_6]$ and $[5(3,5\text{-Py})][PF_6]$ MV derivatives was assigned to a ligand-field (LF) transition in the MV species (also called an interconfigurational (IC) transition by Meyer et al.[4]), by analogy to the absorptions invariably found in related Fe^{III} aryl acetylides.[23] Such a LF transition was also observed for MV complexes containing two weakly coupled $Cp^*(dppe)Fe^{II/III}$ termini.[11,19b,55]

The presence of bands of weak intensities in the NIR region, which does not exist in the spectra of the corresponding homovalent species, clearly establishes that these new complexes constitute original examples of weakly coupled Class II organometallic MV compounds, according to the Robin and Day classification.[17] In previously studied examples, where the two $Cp^*(dppe)Fe^{II/III}$ units are connected by a bridge containing only C and H atoms and even with Si atoms, we noticed that the experimental data collected for these compounds present a high consistency with the two-level Hush model.[11,19b,55] According to this model and within the weak interaction limit, the photoinduced electron transfer gives rise to a single absorption band with a Gaussian shape and the full width of the band at half height obeys eq 4.[5]

Table 10. NIR Data for $[5(2,6\text{-Py})][PF_6]_n$, $[5(3,5\text{-Py})][PF_6]_n$, and $[5(1,3\text{-Ph})][PF_6]_n$ in CH_2Cl_2, Unless Otherwise Specified

compd	transition[a]	ν_{max} (cm^{-1})	ε (M^{-1} cm^{-1})	$(\Delta\nu_{1/2})_{exp}$ (cm^{-1})	$(\Delta\nu_{1/2})_{theo}$[b] (cm^{-1})
$[5(2,6\text{-Py})][PF_6]$	$\{Fe^{II}C\equiv C\text{-py}\rightarrow Fe^{III}C\equiv C\}_{as2}$	4050	240	3600	3059
	LF	5300	55	1100	
	$\{Fe^{II}C\equiv C\rightarrow Fe^{III}C\equiv C\}a_{s1}$	8800	140	3600	
$[5(2,6\text{-Py})][PF_6]$[c]	$\{Fe^{II}C\equiv C\text{-py}\rightarrow Fe^{III}C\equiv C\}_{as2}$	5260	80	3600	3485
	LF	5300	60	1100	
	$\{Fe^{II}C\equiv C\rightarrow Fe^{III}C\equiv C\}_{as1}$	9000	60	3500	
$[5(3,5\text{-Py})][PF_6]$	LF	5450	50	1100	
	$Fe^{II}C\equiv C\rightarrow Fe^{III}C\equiv C$	5450	180	3600	3548
	$Fe^{II}C\equiv C\rightarrow Fe^{III}C\equiv C$	9880	550	5500	
$[5(1,3\text{-Ph})][PF_6]$[d,e]	LF	5350		1050	
	$Fe^{II}C\equiv C\rightarrow Fe^{III}C\equiv C$	5400		3700	3531
	$Fe^{II}C\equiv C\rightarrow Fe^{III}C\equiv C$	10000		3700	
$[5(2,6\text{-Py})][PF_6]_2$	LF	5250	160	1440	
$[5(3,5\text{-Py})][PF_6]_2$	LF	5300	160	1440	
$[5(1,3\text{-Ph})][PF_6]_2$[f]	LF	5460	100	1600	

[a]Assignments based on TD-DFT calculations (see text). [b]Calculated from $(\Delta\nu_{1/2})_{exp} = (2310 \times \nu_{max})^{1/2}$. [c]Acetone. [d]Determined by spectroelectrochemistry (OTTLE cell, 0.1 M tetra-*n*-butylammonium hexafluorophosphate). [e]Results in good agreement with a previous determination on an analogical spectrometer using an isolated sample (see ref 9). [f]From ref 9.

dx.doi.org/10.1021/ic2016148 | Inorg. Chem. 2011, 50, 12601−12622

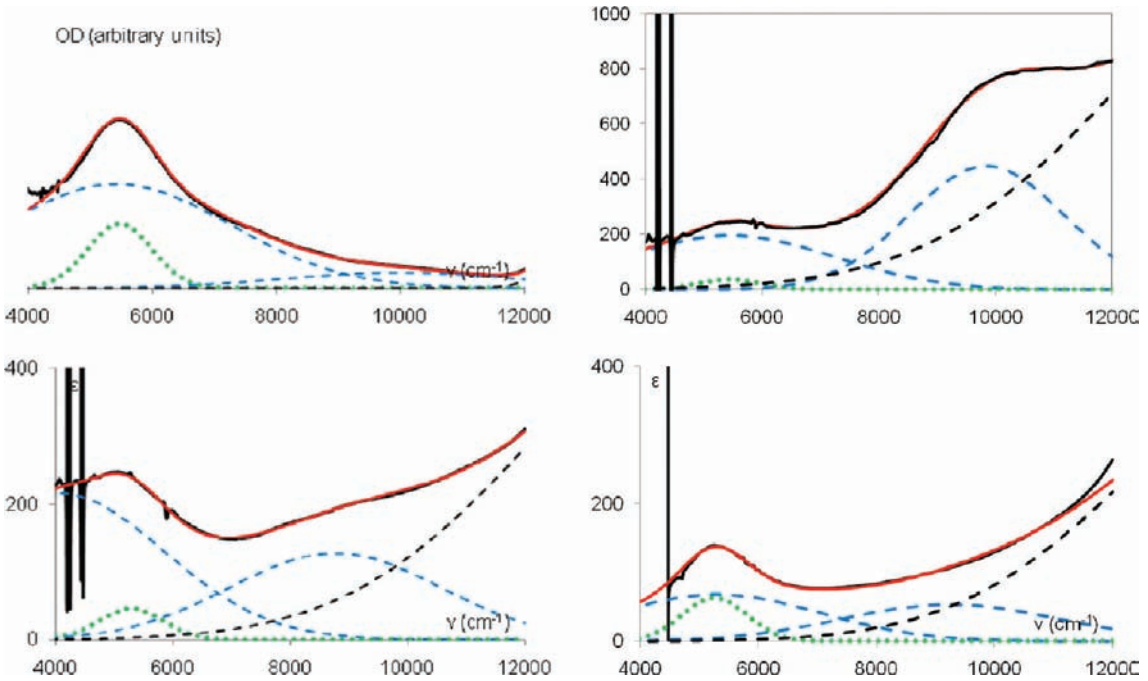

Figure 10. NIR spectra (cm^{-1}) of [**5(1,3-Ph)**][PF_6] (top left in CH_2Cl_2, determined by spectro-electrochemistry, OTTLE cell, absorption in arbitrary units), [**5(3,5-Py)**][PF_6] (top right in CH_2Cl_2), and [**5(2,6-Py)**][PF_6] (bottom left in CH_2Cl_2, bottom right in acetone).

$$\Delta\nu = 2310 \times \nu_{max}{}^{1/2} \quad (4)$$

Moreover, Meyer and co-workers have conclusively shown that inorganic MV complexes possessing several electrons on metal d sublevels might give rise to two additional electron-transfer processes when the metal−metal interaction mediated by the bridge is strong.[4] In this case, the energies of the three optical metal−metal electron transfers are roughly related to the energies of the two LF transitions, according to eqs 5−7. They have the same half-width, and their intensity decreases rapidly as their energy increases.[11,55]

$$E_{IVCT}(1) \approx \lambda \quad (5)$$

$$E_{IVCT}(2) \approx \lambda + E_{LF}(1) \quad (6)$$

$$E_{IVCT}(3) \approx \lambda + E_{LF}(2) \quad (7)$$

These conditions were well-fulfilled in the case of some MV complexes that belong to the same series, namely, [Cp*(dppe)-Fe−C≡C−*B*−C≡C−Fe(dppe)Cp*][PF_6] (*B* = 4,4′-biphenyl;[11] $-(CH_2)_n$ (*n* = 3, 4);[54] or $-(SiMe_2)_n-$, *n* = 2, 3, 4).[55] This is also what we propose for [**5(1,3-Ph)**][PF_6]$_n$ (see Table 6). We also found that the NIR spectrum of this MV complex is almost solvent-independent.[9] For this reason, we carefully compared the NIR spectra obtained in CH_2Cl_2 and acetone of the three MV complexes [**5(2,6-Py)**][PF_6], [**5(3,5-Py)**][PF_6], and [**5(1,3-Ph)**][PF_6]. The intensities of all bands (except those assigned to LF transitions) are very sensitive to the solvent polarity and they almost vanish in acetone. However, the complexes [**5(3,5-Py)**][PF_6] and [**5(1,3-Ph)**][PF_6] behave similarly and the energy of the different bands are only very weakly sensitive to the polarity of the solvent. In contrast, in the case of the complex [**5(2,6-Py)**][PF_6], the band located on the low-energy side (4050 cm^{-1} in CH_2Cl_2) shift to 5260 cm^{-1} in acetone. This different solvatochromism suggests that this band may have a different origin.

For the MV complexes [**5(3,5-Py)**][PF_6] and [**5(1,3-Ph)**][PF_6], the two bands located at ∼5400 and 9500 cm^{-1} can be tentatively assigned to Fe^{II}−C≡C → Fe^{III}−C≡C transitions, based on the DFT calculations (see above). In the case of the MV [**5(2,6-Py)**][PF_6], with the time scale of the NIR spectroscopy being faster than that of the IR, bands corresponding to both **as1** and **as2** isomers are expected to be observed. With the support of theory, the band at lower energy might be assigned to a Fe^{II}−C≡C−Py → Fe^{III}−C≡C transition in the **as2** isomer, while the high-energy band should correspond to a Fe^{II}−C≡C → Fe^{III}−C≡C transition in the **as1** isomer (see above).

Considering the small intramolecular electron-transfer rates established from Mössbauer data ($k_e < 10^{-6}$ s), the absence of solvatochromism of the intervalence charge transfer (IT) bands found for [**5(3,5-Py)**][PF_6] and [**5(1,3-Ph)**][PF_6] is surprising. Indeed, for these trapped MV complexes, the IT bands are expected to be solvent-dependent. However, MV derivatives with solvent-independent energies for IT bands are not unprecedented. This scenario arises when the time scale for reorganization of the solvent is faster than that for the inner-sphere vibrations, giving rise to solvent averaging and electronic localization, which is not the case here.[4,61] The solvent dependence observed in the case of [**5(2,6-Py)**][PF_6] is not easier to understand. In this case, comparison of the IR spectra run in CH_2Cl_2 and acetone suggests that interconversion between the isomers **as1** and **as2** is probably faster in the former solvent. As a consequence, electron transfer might not occur via the same pathways in both solvents.

Overall, our data cannot be rationalized by the oversimplified two-state model as we did for many other MV containing the same redox-active Fe centers. A three-state model with a mediating state formed by a charge transfer from the bridging

dx.doi.org/10.1021/ic2016148 | *Inorg. Chem.* 2011, 50, 12601−12622

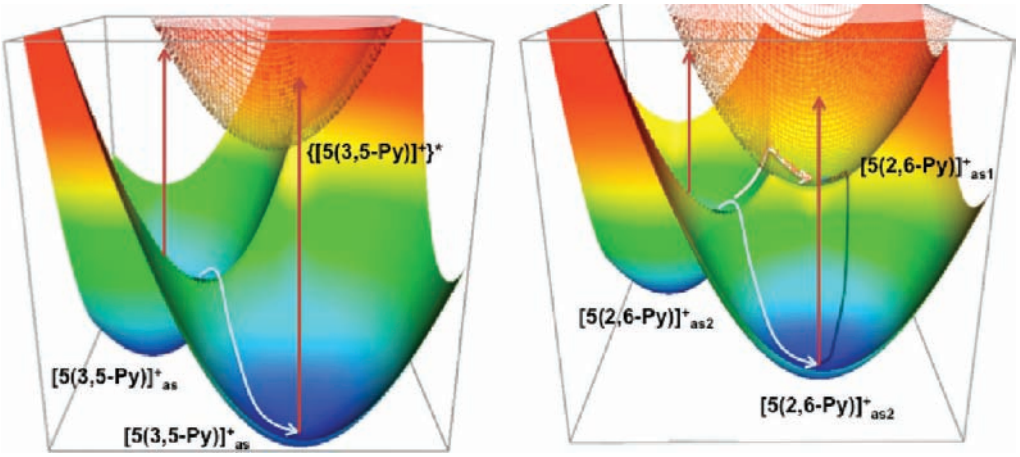

Figure 11. Schematic representation of the energy profile for $[\mathbf{5(3,5\text{-}Py)}]^{+}_{as}$ (left, eq 9 satisfied, * = excited state), and $[\mathbf{5(2,6\text{-}Py)}]^{+}_{as2}$ (right, eq 10 satisfied), made using the *Grapher* program; *x*-axis = reaction coordinate Q_1, *y*-axis = reaction coordinate Q_2, *z*-axis = energy.

group (eq 8) appears more appropriate in the present case. Indeed, beside the LF transition, the NIR spectra of the MV the $\mathbf{5}[\mathbf{PF_6}]$ series displays two bands with almost-Gaussian shapes, but with relative intensities different from those found for the related MV derivatives $\mathbf{1}-\mathbf{7}[\mathbf{PF_6}]$. In particular, the relative intensity of the bands in the NIR spectrum of $[\mathbf{5(2,6\text{-}Py)}][\mathbf{PF_6}]$ is ~0.58, which is too large to be consistent with a LF/IVCT coupling. In the case of $[\mathbf{5(3,5\text{-}Py)}][\mathbf{PF_6}]$, the band at the highest energy (9880 cm^{-1}) is three times more intense than the band located at 5450 cm^{-1}.

$$M^{+} - B - M \rightarrow M - B^{+} - M \rightarrow M - B - M^{+} \quad (8)$$

$$\Delta G^{0}_{ac} \approx \lambda_{LMCT} > \lambda_{IVCT} \quad (9)$$

$$\Delta G^{0}_{ac} < \lambda_{LMCT} < \lambda_{IVCT} \quad (10)$$

The impact of the third state is dependent on its energy, relative to the other two diabatic states.[5,62] Two critical situations may happen: The free energy of the mediating state (G^{0}_{c}) lies above or just below the intersection of the reactant and product diabatic states, as shown in Figure 11 (see also Figures 11 and 12 in ref 5). In the first case, the third state lies above the intersection of the reactant (G^{0}_{a}) and product (G^{0}_{b}) diabatic states and the conditions defined in eq 9 are fulfilled. When eq 9 is satisfied, the MMCT band is located at a lower energy than the LMCT band. The intermediate excited state lies above a minimum of energy of the ground state and relaxation process provides exclusively the Fe^{II}/Fe^{III} localized system. This is probably the situation encountered for $[\mathbf{5(3,5\text{-}Py)}][\mathbf{PF_6}]$ and $[\mathbf{5(1,3\text{-}Ph}][\mathbf{PF_6}]$, as well as for $[\mathbf{5(2,6\text{-}Py)}][\mathbf{PF_6}]_{as1}$. As a consequence, the charge is metal-centered and only species with well-identified Fe^{II} and Fe^{III} centers can spectroscopically be characterized, regardless of the time scale of the methods.

In the second case, which might correspond to the energy profile of $[\mathbf{5(2,6\text{-}Py)}][\mathbf{PF_6}]_{as2}$, conditions defined in eq 10 are obeyed and the diabatic mediating state lies just below the reactant and product diabatic states and the LMCT transition should be less energetic than the MMCT transition. Here, the direct coupling does not occur ($H_{ab} = 0$) and only the coupling between the bridge (c) and the reactant and product (a, b) diabatic states is considered ($H_{ac} = H_{bc}$). In this case, the middle adiabatic state can develop a minimum of energy between reactant and product states which can be of sufficient stability to be populated as an intermediate and, therefore, are observed with a spectroscopic means, with a time scale consistent with its lifetime.

CONCLUSION

This theoretical and experimental study on the nitrogen-substituted $[2,6\text{-}\{Cp^{*}(dppe)Fe{-}C{\equiv}C{-}\}_2(C_5H_3N)][PF_6]_n$ ($[\mathbf{5(2,6\text{-}Py)}][\mathbf{PF_6}]_n$) and $[3,5\text{-}\{Cp^{*}(dppe)Fe{-}C{\equiv}C{-}\}_2(C_5H_3N)][PF_6]_n$ ($[\mathbf{5(3,5\text{-}Py)}][\mathbf{PF_6}]_n$) complexes and the reference derivatives $[1,3\text{-}\{Cp^{*}(dppe)Fe{-}C{\equiv}C{-}\}_2(C_5H_4)][PF_6]_n$ ($[\mathbf{5(1,3\text{-}Ph)}][\mathbf{PF_6}]_n$), with n = 0–2, shows how the physical properties are distinctively influenced by the presence of a N atom in the central bridging ligand. The geometries and electronic structure of the neutral systems are rather similar, but the vibrational spectra have a distinct signature in each case, like a fingerprint. This work allows us to demonstrate the following:

(i) With respect to the reference compound $\mathbf{5(1,3\text{-}Ph)}$, insertion of a N atom in the short branch of the aryl ring increases the difference between the two redox potentials (ΔE^{0}), while ΔE^{0} decreases when nitrogen is placed in a symmetric position of the long branch.

(ii) The presence of the N atom makes the mono-oxidized and dioxidized species more reactive than the corresponding reference compounds, but, nevertheless, all the oxidized forms were isolated and characterized as hexafluorophosphate salts.

(iii) The presence of the N atom in the long branch increases the ferromagnetic interaction between the two Fe^{III} spin carriers, whereas, if placed in the short branch, it dramatically reduces the magnetic exchange.

(iv) The MV complexes are all trapped and belong to the Robin–Day Class II compounds, as evidenced by MR-CI results and confirmed experimentally by Mössbauer spectroscopy.

(v) When the N atom is located in the small branch, two rotamers of the MV species with different charge distributions can be observed and their exchange rate is slow at the fast IR time scale. Indeed, the computational studies strongly establish that spin localization is dependent on the conformation of the molecule.

(vi) Electron transfer probably occurs via different pathways for these two rotamers.

dx.doi.org/10.1021/ic2016148 | *Inorg. Chem.* 2011, 50, 12601–12622

(vii) When the N atom is positioned on the long branch, the intermediate excited state is higher in energy than the ground-state conformers and the relaxation process provides the Fe^{II}/Fe^{III} localized system exclusively ($H_{ab} \neq 0$).

Localization of the N atom on the short branch modifies the energy profile. The diabatic mediating state is stable enough to have the metal-to-metal charge transfer (MMCT) transition less energetic than the ligand-to-metal charge transfer (LMCT). Here, the direct coupling does not occur ($H_{ab} = 0$) and mediating state (c) implies that the bridge is involved in the charge transfer process between the reactant (a) and product (b) diabatic states ($H_{ac} = H_{bc}$).

EXPERIMENTAL SECTION

Computational Details. DFT calculations were carried out with the Gaussian 03 program.[63] The geometric structures were fully optimized without any symmetry constraint, using the B3LYP[64] functional within the LANL2DZ ECP basis set, augmented by a polarization function for all atoms except H.[65] Harmonic vibrational frequency calculations were performed to check that the optimized geometries were energy minima. The guess functions of the valence-localized and broken-symmetry systems were generated with the Jaguar 6.0 code.[66] The isosurface spin-density representations were done using the MOLEKEL program.[67]

CAS-SCF[68] and MR-CI[69] calculations were performed using the Molpro 2009 program suite.[70] In the case of MR-CI computations, the internal contracted formalism, as developed in MOLPRO, was used. All computations were carried out with the minimal STO-3G basis,[71] because of the quite-important computational cost of CAS-SCF and especially MR-CI computations (see the Supporting Information). The use of multireference CAS-SCF wave function allowed us to straightforwardly compute the energy spectrum of the ground state and the first five electronic excited states of the symmetrical and asymmetrical complexes. Geometries of the two conformations were taken from the lowest-energy optimized symmetrical and the most asymmetrical DFT structures. No other geometry optimization was attempted; therefore, the spectra can be considered to be composed of vertical excitations from the optimized DFT geometries.

General. Manipulations of air-sensitive compounds were performed under an argon atmosphere, using standard Schlenk techniques or in an argon-filled Jacomex 532 drybox. All glassware was oven-dried and vacuum or argon flow-degassed before use. Fourier transform infrared (FT-IR) spectra were recorded using a Bruker Model IFS28 spectrophotometer (range of 4000−400 cm^{-1}) as solids dispersed in KBr pellets. UV−visible spectra were recorded on an UVIKON XL spectrometer. ^{1}H, ^{13}C, and ^{31}P NMR spectra were recorded on a Bruker Model DPX200 NMR multinuclear spectrometer at ambient temperature, unless otherwise noted. Chemical shifts are reported in parts per million (δ), relative to tetramethylsilane ($Si(CH_3)_4$) for ^{1}H, and ^{13}C NMR spectra, and external 85% H_3PO_4 for ^{31}P NMR spectra. Coupling constants (J) are reported in units of Hertz (Hz), and integrations are reported as number of protons. The following abbreviations are used to describe peak patterns: br = broad, s = singlet, d = doublet, t = triplet, q = quartet, and m = multiplet. Mass spectra were run on a Hewlett−Packard Model HP 5971/A/5890-II GC/MS coupling (HP 1 capillary column, length = 25 m, diameter = 0.2 mm, 0.33 μm polydimethylsiloxane). EPR spectra were recorded on a Bruker Model EMX-8/2.7 (X-band) spectrometer equipped with liquid nitrogen cryostat. Cyclic voltammograms were recorded using a PAR 263 instrument in CH_2Cl_2 (0.1 M $[NBu_4]PF_6$) at 25 °C with a platinum electrode, using a SCE reference electrode and ferrocene as an internal calibrant (0.460 V).[72] The ^{57}Fe Mössbauer spectra were recorded with a 2.5×10^{-2} C (9.25×10^{8} Bq) ^{57}Co source, using a symmetric triangular sweep mode. Computer fitting of the Mössbauer data to Lorentzian line shapes was carried out with a previously reported computer program.[45] The isomer shift values are reported relative to iron foil at 298 K.[45] The magnetization was recorded with a Quantum Design MPMS SQUID magnetometer operating in the temperature range of 2−300 K with a DC magnetic field up to 5 T. The experimental data have been corrected from the diamagnetism of the sample holder, and the intrinsic diamagnetism of the materials have been evaluated with Pascal's tables. Elemental analyses were conducted on a Thermo-FINNIGAN Flash EA 1112 CHNS/O analyzer by the Microanalytical Service of the Centre Régional de Mesures Physiques de l'Ouest (CRMPO) at the University of Rennes 1, France.

Materials. Reagent-grade toluene, tetrahydrofuran (THF), diethyl ether, and pentane were dried and deoxygenated by distillation from sodium/benzophenone ketyl. Dichloromethane was distilled under argon from P_2O_5 and then from Na_2CO_3. Cp*(dppe)FeCl,[73] $[(C_5H_5)_2Fe][PF_6]$ (ferrocenium hexafluorophosphate),[72] and $[(C_5H_5)_2Fe][BPh_4]$ (ferrocenium tetraphenylborate)[72] were prepared following published procedures.

{Cp*(dppe)Fe(C≡C)}$_2$(2,6-C_5H_4N) (5(2,6-Py)). Two methods were used; they will be referenced as Method A and Method B.

In Method A, a Schlenk tube was charged with 0.395 g (1.45 mmol) of 2,6-bis(trimethylsilylethynyl)pyridine, 2.000 g (3.2 mmol) of Cp*(dppe)FeCl, 0.586 g (3.2 mmol) of KPF_6, and 0.189 g of KF, before the addition of 50 mL of MeOH. The green mixture was reacted for 16 h at 20 °C and turned slowly purple. Then, 0.376 g (3.2 mmol) of $KOBu^t$ was added and the solution immediately became orange. The solvent was removed to dryness and the solid residue was extracted with toluene (3 × 20 mL). After removal of the solvent and drying under vacuum, the orange powder was washed with pentane (10 mL). Upon vacuum drying, 1.850 g (1.42 mmol, 98%) of orange powder was obtained. Crystals were grown from the slow diffusion of pentane into dichloromethane.

In Method B, a Schlenk tube was charged with 0.295 g (1.1 mmol) of 2,6-bis(trimethylsilylethynyl)pyridine, 1.500 g (2.4 mmol) of Cp*(dppe)FeCl, 0.586 g (2.4 mmol) of K_2CO_3, 0.818 g (2.4 mmol) of $NaBPh_4$, and 50 mL of MeOH. This green mixture was stirred under reflux for 16 h and, after cooling to room temperature, 0.269 g (2.4 mmol) of $KOBu^t$ was added, after which the solvent was evaporated and the residue was extracted with toluene (4 × 10 mL). After removal of the solvent, washing with pentane (3 × 10 mL), and vacuum drying, 1.120 g (0.87 mmol, 79%) of an orange powder were obtained.

Anal. Calcd for $C_{81}H_{81}Fe_2NP_4$, 0.5 CH_2Cl_2 (crystallization solvent): C, 72.69; H, 6.14; N, 1.04. Found: C, 72.68; H, 6.32; N, 1.20. ESI MS (m/z): calcd for $C_{81}H_{82}P_4N_{56}Fe_2$, 1304.4097; found, 1304.4039 $[M + H]^+$. ^{1}H NMR (200 MHz, C_6D_6): δ 8.20−7.00 (m, 41H, Ar*H* + pyr H-4); 6.79 (d, 2H, $^{3}J_{HH}$ = 7.6 Hz, pyr H-3, 5), 2.97, 1.90 (2 m, 8H, CH_2/dppe), 1.54 (s, 30H, Cp*). ^{13}C NMR (75 MHz, C_6D_6): δ 147.7 (s, pyr-C-4); 140.3−127.4 (m, Ar*C*), 138.7 (t, $^{2}J_{CP}$ = 39 Hz, Fe−*C*≡C), 128.3 (s, pyr C-3, 5), 123.1 (m, ^{3}JCP = 2 Hz, FeC≡*C*), 119.5 (s, pyr C-4), 88.0 (s, Cp*), 31.4 (m, CH_2/dppe), 10.6 (s, Cp*). $^{31}P\{^{1}H\}$ NMR (81 MHz, C_6D_6): δ 102.1 (s, dppe). IR (Nujol, cm^{-1}): ν 2048 (s, C≡C), 1558 (m, Py), 1548 (w, Py), 1538 (m, Py); (CH_2Cl_2, cm^{-1}): ν =2043 (s, C≡C), 1559 (m, Py), 1551 (w, Py), 1539 (m, Py).

{Cp*(dppe)Fe(C≡C)}$_2$(3,5-C_5H_4N) (5(3,5-Py)). A Schlenk tube was charged with 0.181 g (0.66 mmol) of 2,6-bis-(trimethylsilylethynyl)pyridine, 0.221 g (1.6 mmol) of K_2CO_3, and 40 mL of MeOH. The solution was reacted for 16 h at 20 °C, and then 1.000 g (1.60 mmol) of Cp*(dppe)FeCl and 0.549 g (1.60 mmol) of $NaBPh_4$ were added. Upon reflux for 8 h, the suspension turned orange. After cooling to room temperature, 0.180 g of $KOBu^t$ (1.60 mmol) was added and the mixture was stirred for 15 min. The solvent then was evaporated and the solid residue was extracted with CH_2Cl_2 (3 × 10 mL). After removal of the solvent, washing with pentane (4 × 10 mL), and vacuum drying, 0.760 g (0.58 mmol, 88%) of an orange powder was obtained. Anal. Calcd for $C_{81}H_{81}Fe_2NP_4$, 0.5 CH_2Cl_2 (crystallization solvent): C, 72.69; H, 6.14. Found: C, 72.64; H, 6.13. ESI MS (m/z): calcd for $C_{81}H_{81}P_4N_{56}Fe_2$, 1303.4018; found, 1303.3985 $[M]^+$. ^{1}H NMR (200 MHz, C_6D_6): δ 8.43 (d, 2H, $^{4}J_{HH}$ = 1.7 Hz, pyr H-2, 6), 8.03−7.06 (m, 41H, Ar*H*, pyr H-4), 2.60, 1.83 (2 m, 8H, CH_2/dppe), 1.52 (s, 30H, Cp*). ^{13}C NMR (75 MHz,

dx.doi.org/10.1021/ic2016148 | Inorg. Chem. 2011, 50, 12601−12622

C_6D_6): δ 146.8 (dm, $^1J_{CH}$ = 177 Hz, pyr C-2, 6), 140.7 (t, $^2J_{CP}$ = 39 Hz, Fe−C≡C), 140.1−127.5 (m, Ar/dppe), 136.9 (dm, $^1J_{CR}$ = 165 Hz, pyr C-4), 126.9 (m, pyr C-3, 5), 117.3 (s, Fe−C≡C), 87.9 (s, Cp*), 31.2 (m, CH_2/dppe), 10.5 (q, $^1J_{CH}$ = 126 Hz, Cp*). ^{31}P NMR (81 MHz, C_6D_6): δ = 101.6 (s, dppe). IR (Nujol, cm^{-1}): ν = 2042 (s, C≡C), 1586 (w, Py), 1555 (m, Py); (CH_2Cl_2, cm^{-1}): ν = 2044 (s, C≡C), 1586 (w, Py), 1557 (m, Py).

[{Cp*(dppe)Fe(C≡C)}$_2$(2,6-C_5H_4N)][PF_6]$_2$ [(5(2,6-Py)][PF_6]$_2$. A solution of **5(2,6-Py)** (0.523 g, 0.40 mmol) in THF (20 mL) was cooled at −60 °C, and then 1.95 equiv of ferrocenium hexafluorophosphate was added (0.259 g, 0.78 mmol). The solution was stirred for 16 h at this temperature and then concentrated to 5 mL. A gray powder was precipitated from the solution via the addition of pentane (40 mL). After removal of the solvent, washing with pentane (3 × 10 mL), and vacuum drying 0.620 g (0.39 mmol, 97%), [**5(2,6-Py)**][PF_6]$_2$ was isolated as a gray powder and characterized by a CV identical to **5(2,6-Py)**, using IR, UV−vis, NIR, EPR, and Mössbauer spectroscopy.

[{Cp*(dppe)Fe(C≡C)}$_2$(3,5-C_5H_4N)][PF_6]$_2$ [(5(3,5-Py)][PF_6]$_2$. A solution of **5(3,5-Py)** (0.354 g, 0.27 mmol) in THF (20 mL) was cooled at −60 °C, and then 1.95 equiv of ferrocenium hexafluorophosphate was added (0.175 g, 0.53 mmol). The solution was stirred for 16 h at this temperature and then concentrated to 5 mL. A black powder was precipitated from the solution via the addition of pentane (30 mL). After removal of the solvent, washing with pentane (3 × 10 mL), and vacuum drying, 0.400 g (0.25 mmol, 93%) of [(**5(3,5-Py)**][PF_6]$_2$ was isolated as a black powder and characterized by a CV identical to **5(3,5-Py)**, using IR, UV−vis, NIR, EPR, and Mössbauer spectroscopy.

[{Cp*(dppe)Fe(C≡C)}$_2$(2,6-C_5H_4N)][PF_6] [(5(2,6-Py)][PF_6]). A Schlenk tube was charged with [(**5(2,6-Py)**] (0.045 g, 0.035 mmol) and [(**5(2,6-Py)**][PF_6]$_2$ (0.055 g, 0.035 mmol) and 30 mL of THF. After stirring for 15 min at 20 °C, the solution turned to yellow green very quickly. After removal of the solvent, washing with pentane (3 × 10 mL), and vacuum drying, 0.090 g (0.32 mmol, 93%) of [(**5(3,5-Py)**][PF_6] was isolated as a black powder and characterized by a CV identical to **5(2,6-Py)**, using IR, UV−vis, NIR, EPR, and Mössbauer spectroscopy.

[{Cp*(dppe)Fe(C≡C)}$_2$(3,5-C_5H_4N)][PF_6] [(5(3,5-Py)][PF_6]). A Schlenk tube was charged with [(**5(3,5-Py)**] (0.045 g, 0.035 mmol) and [(**5(3,5-Py)**][PF_6]$_2$ (0.055 g, 0.035 mmol) and 30 mL of THF. After stirring for 15 min at 20 °C, the solution turned to yellow green very quickly. After removal of the solvent, washing with pentane (3 × 10 mL), and vacuum drying, 0.090 g (0.32 mmol, 93%) of [(**5(3,5-Py)**][PF_6] was isolated as a black powder and characterized by a CV identical to **5(3,5-Py)**, using IR, UV−vis, NIR, EPR, and Mössbauer spectroscopy.

Crystallography. Data collection of crystals of **5(2,6-Py)** was performed on a Bruker Model AXS X8-APEX II Oxford Diffraction system at 100 K, while data collection for **5(3,5-Py)** was performed on an Xcalibur Saphir 3 diffractometer at 293 K, both with graphite monochromatized Mo Kα radiation. The cell parameters (Table 5) were obtained using Denzo and Scalepack software.[74] The data collection ($2\theta_{max}$ = 54°; phi scan frames via 1.0° phi rotation and 20 s per frame; *hkl* range: *h* 0.28, *k* 0.25, *l* −34.38 for **5(3,5-Py)**;[75] and $2\theta_{max}$ = 54°; omega scan frames via 0.75° omega rotation and 30 s per frame; *hkl* range: *h* 0.11, *k* −23.23, *l* −31.31 for **5(3,5-Py)**[76]) provided a crude set of reflections from which the independent reflections were obtained after data reduction.[74] The structures were solved with SIR-97, which revealed the non-hydrogen atoms.[77] After anisotropic refinement, the remaining atoms were found in Fourier difference maps. The complete structures were then refined with SHELXL97,[78] using the full-matrix least-squares technique (use of F square magnitude, giving the following: for **5(2,6-Py)**: *x*, *y*, *z*, β_{ij} for Fe, P, C, and N atoms, *x*, *y*, *z* in riding mode for H atoms; 1585 variables and 12894 observations with $I > 2.0\sigma(I)$; calc $w = 1/[\sigma^2(F_o^2) + (0.08P)^2]$, where $P = (F_o^2 + 2F_c^2)/3$; and for **5(3,5-Py)**: *x*, *y*, *z*, β_{ij} for Fe, P, N, and C atoms, *x*, *y*, *z* in riding mode for H atoms; 852 variables and 10437 observations with $I > 2.0\sigma(I)$; calc $w = 1/[\sigma^2(F_o^2) + (0.10P)^2]$, where $P = (F_o^2 + 2F_c^2)/3$). Atomic scattering factors were taken from the literature.[79] ORTEP views of **5(2,6-Py)** and **5(3,5-Py)** were realized with PLATON98.[80] Final atomic positional coordinates, with estimated standard deviations, bond lengths, and angles, in addition to anisotropic thermal parameters, have been deposited at the Cambridge Crystallographic Data Centre and were allocated the deposition numbers CCDC 273845 and CCDC 292381, respectively.

■ ASSOCIATED CONTENT

Ⓢ Supporting Information

Crystallographic (CIF) files for **5(2,6-Py)** and **5(3,5-Py)**. Optimized Cartesian coordinates of all studied compounds. TD-DFT calculations of [**5H(2,6-Py)**]$^{n+}$, [**5H(3,5-Py)**]$^{n+}$, and [**5H(1,3-Ph)**]$^{n+}$ (n = 0, 1). MR-CI active space. X-band EPR of [**5(2,6-Py)**][PF_6]$_n$ and [**5(3,5-Py)**][PF_6]$_n$ (n = 1, 2). Cyclic voltammograms of **5(2,6-Py)**, **5(3,5-Py)**, and **5(1,3-Ph)**. UV−visible spectra of [**5(2,6-Py)**]$^{n+}$ and [**5(3,5-Py)**]$^{n+}$ (n = 0, 1, 2). This material is available free of charge via the Internet at http://pubs.acs.org.

■ AUTHOR INFORMATION

Corresponding Author

*E-mails: kcostuas@univ-rennes1.fr (K.C.); claude.lapinte@univ-rennes1.fr (C.L.); and halet@univ-rennes1.fr (J.-F.H.).

■ ACKNOWLEDGMENTS

This work was performed using the high-performance computing resources from GENCI-CINES and GENCI-IDRIS (Grant No. 2010-80649).

■ REFERENCES

(1) (a) Crutchley, R. J. *Adv. Inorg. Chem.* **1994**, *41*, 273−325. Ward, M. D. *Chem. Soc. Rev.* **1995**, *24*, 121−134. (b) Ward, M. D. *Chem. Ind.* **1996**, 568−573.

(2) Paul, F.; Lapinte, C. *Coord. Chem. Rev.* **1998**, *178−180*, 427−505.

(3) Paul, F.; Lapinte, C. Magnetic communication in binuclear organometallic complexes mediated by carbon-rich bridges. In *Unusual Structures and Physical Properties in Organometallic Chemistry*; Gielen, M., Willem, R., Wrackmeyer, B., Eds.; John Wiley & Sons, Ltd.: London, 2002; pp 220−291.

(4) Demandis, K. D.; Hartshorn, C. M.; Meyer, T. J. *Chem. Rev.* **2001**, *101*, 2655−2685.

(5) Brunschwig, B. S.; Creutz, C.; Sutin, N. *Chem. Soc. Rev.* **2002**, *31*, 168−184.

(6) Akita, M.; Koike, T. *Dalton Trans.* **2008**, 3523−3530.

(7) Le Narvor, N.; Toupet, L.; Lapinte, C. *J. Am. Chem. Soc.* **1995**, *117*, 7129−7138.

(8) Lapinte, C. *J. Organomet. Chem.* **2008**, *693*, 793−801.

(9) Weyland, T.; Costuas, K.; Toupet, L.; Halet, J.-F.; Lapinte, C. *Organometallics* **2000**, *19*, 4228−4239.

(10) Lu, Y.; Quardokus, R.; Lent, C. S.; Justaud, F.; Lapinte, C.; Kandel, S. A. *J. Am. Chem. Soc.* **2010**, *132*, 13519−13524.

(11) Ghazala, S. I.; Paul, F.; Toupet, L.; Roisnel, T.; Hapiot, P.; Lapinte, C. *J. Am. Chem. Soc.* **2006**, *128*, 2463−2476.

(12) Le Stang, S.; Paul, F.; Lapinte, C. *Organometallics* **2000**, *19*, 1035−1043.

(13) de Montigny, F.; Argouarch, G.; Costuas, K.; Halet, J.-F.; Roisnel, T.; Toupet, L.; Lapinte, C. *Organometallics* **2005**, *24*, 4558−4572.

(14) Costuas, K.; Rigaut, S. *Dalton Trans.* **2011**, *40*, 5643−5658.

(15) (a) Hush, N. S. *Prog. Inorg. Chem.* **1967**, *8*, 391−444. (b) Marcus, R. A.; Sutin, N. *Biochim. Biophys. Acta* **1985**, *811*, 265−322. (c) Day, P.; Hush, N. S.; Clark, R. J. H. *Philos. Trans. R. Soc.* **2008**, *A366*, 5−14.

(16) D'Alessandro, D. M.; Keene, F. R. *Chem. Soc. Rev.* **2006**, *35*, 424−440.

(17) Robin, M. B.; Day, P. *Adv. Inorg. Chem. Radiochem.* **1967**, *10*, 247−422.
(18) Le Narvor, N.; Lapinte, C. *C. R. Acad. Sci., Ser. IIc: Chim.* **1998**, 745−749. See also ref 57.
(19) (a) Roué, S.; Le Stang, S.; Toupet, L.; Lapinte, C. *C. R. Chim.* **2003**, *6*, 353−366. (b) Weyland, T.; Ledoux, I.; Brasselet, S.; Zyss, J.; Lapinte, C. *Organometallics* **2000**, *19*, 5235−5237.
(20) Patoux, C. C.; Launay, J.-P.; Joachim, C.; Gourdon, A. *Inorg. Chem.* **1997**, *36*, 5037−5049. See also ref 57.
(21) Ami, S.; Joachim, C. *Phys. Rev. B* **2002**, *65*, 155419.
(22) Tanaka, Y.; Shaw-Taberlet, J. A.; Justaud, F.; Cador, O.; Roisnel, T.; Akita, M.; Hamon, J.-R.; Lapinte, C. *Organometallics* **2009**, *28*, 4656−4669.
(23) Paul, F.; Toupet, L.; Thépot, J.-Y.; Costuas, K.; Halet, J.-F.; Lapinte, C. *Organometallics* **2005**, *24*, 5464−5478.
(24) Lundberg, T. M.; Siegbahn, P. E. *J. Chem. Phys.* **2005**, *122*, 224103−9.
(25) Ruiz, E.; Alvarez, S.; Cano, J.; Polo, V. *J. Chem. Phys.* **2005**, *123*, 164110.
(26) Cohen, A. J.; Mori-Sánchez, P.; Yang, W. *Science* **2008**, *321*, 792−794.
(27) Hybrid functionals containing too much HF exchange can lead to incorrect results, favoring too much "localization".
(28) (a) Wu, Q.; Van Voorhis, T. *Phys. Rev. A* **2005**, *72*, 0245021−0245024. (b) Wu, Q.; Van Voorhis, T. *J. Chem. Theory Comput.* **2006**, *2*, 765−774.
(29) Costuas, K.; Paul, F.; Toupet, L.; Halet, J.-F.; Lapinte, C. *Organometallics* **2004**, *23*, 2053−2068.
(30) (a) Schilling, B. E. R.; Hoffmann, R.; Lichtenberger, D. L. *J. Am. Chem. Soc.* **1979**, *101*, 585−591. (b) Bruce, M. I.; Low, P. J.; Costuas, K.; Halet, J.-F.; Best, S. P.; Heath, G. A. *J. Am. Chem. Soc.* **2000**, *122*, 1949−1962.
(31) Let us recall that the electronic structure of the latter should show two unpaired electrons with opposite spin in different spin−orbitals (SO) localized on one-half of the molecule.
(32) Nair, N. N.; Schreiner, E.; Pollet, R.; Staemmler, V.; Marx, D. *J. Chem. Theory Comput.* **2008**, *4*, 1174−1188.
(33) (a) Nishino, M.; Yamanaka, S.; Yoshioka.; Yamaguchi, K. *J. Phys. Chem. A* **1997**, *101*, 705−712. (b) Yamaguchi, K.; Fukui, H.; Fueno, T. *Chem. Lett.* **1986**, 625−628.
(34) (a) Ruiz, E.; Cano, J.; Alvarez, S.; Alemany, P. *J. Comput. Chem.* **1999**, 1391−1400. (b) Ruiz, E.; Alvarez, S.; Cano, J.; Polo, V. *J. Chem. Phys.* **2006**, *124*, 107102.
(35) Yu, L.; Srinivas, G. N.; Schwartz, M. *J. Mol. Struct. (THEOCHEM)* **2003**, *625*, 215−220.
(36) Tilset, M.; Fjeldahl, I.; Hamon, J.-R.; Hamon, P.; Toupet, L.; Saillard, J.-Y.; Costuas, K.; Haynes, A. *J. Am. Chem. Soc.* **2001**, *123*, 9984−10000.
(37) (a) Monari, A.; Evangelisti, S.; Leininger, T. *J. Chem. Phys.* **2010**, *133*, 124301−8. (b) Helal, W.; Evangelisti, S.; Leininger, T.; Maynau, D. *J. Comput. Chem.* **2009**, *30*, 83−92. (c) Helal, W.; Monari, A.; Evangelisti, S.; Leininger, T. *J. Phys. Chem. A* **2009**, *113*, 5240−5245.
(38) Weyland, T.; Lapinte, C.; Frapper, G.; Calhorda, M. J.; Halet, J.-F.; Toupet, L. *Organometallics* **1997**, *16*, 2024−2031.
(39) Bruce, M. I. *Chem. Rev.* **1991**, *91*, 197−257.
(40) Wu, I. Y.; Lin, J. T.; Luo, J.; Sun, S.-S.; Li, C.-S.; Lin, K. J.; Tsai, C.; Hsu, C.-C.; Lin, J.-L. *Organometallics* **1997**, *16*, 2038−2048.
(41) (a) Justaud, F.; Argouarch, G.; Ghazala, S. I.; Toupet, L.; Paul, F.; Lapinte, C. *Organometallics* **2008**, *27*, 4260−4264. (b) Paul, F.; Goeb, S.; Justaud, F.; Argouarch, G.; Toupet, L.; Ziessel, R.; Lapinte, C. *Inorg. Chem.* **2007**, *46*, 9036−9038. (c) Justaud, F.; Roisnel, T.; Lapinte, C. *New J. Chem.* **2011**, DOI: 10.1039/c1nj20269c.
(42) Le Narvor, N.; Lapinte, C. *Organometallics* **1995**, *14*, 634−639.
(43) (a) Connelly, N. G.; Gamasa, M. P.; Gimeno, J.; Lapinte, C.; Lastra, E.; Maher, J. P.; Le Narvor, N.; Rieger, A. L.; Rieger, P. H. *J. Chem. Soc., Dalton Trans.* **1993**, 2575−2578. (b) Denis, R.; Toupet, L.; Paul, F.; Lapinte, C. *Organometallics* **2000**, *19*, 4240−4251.
(44) Le Stang, S.; Paul, F.; Lapinte, C. *Inorg. Chim. Acta* **1999**, *291*, 403−425.
(45) Varret, F.; Mariot, J.-P.; Hamon, J.-R.; Astruc, D. *Hyperfine Interact.* **1988**, *39*, 67−81.
(46) Guillaume, V.; Thominot, P.; Coat, F.; Mari, A.; Lapinte, C. *J. Organomet. Chem.* **1998**, *565*, 75−80.
(47) Argouarch, G.; Thominot, P.; Paul, F.; Toupet, L.; Lapinte, C. *C. R. Chim.* **2003**, *6*, 209−222.
(48) Weyland, T.; Costuas, K.; Mari, A.; Halet, J.-F.; Lapinte, C. *Organometallics* **1998**, *17*, 5569−5579.
(49) Paul, F.; Malvoti, F.; da Costa, G.; Le Stang, S.; Justaud, F.; Argouarch, G.; Bondon, A.; Sinbandhit, S.; Costuas, K.; Toupet, L.; Lapinte, C. *Organometallics* **2010**, *29*, 2491−2502.
(50) (a) Greenwood, N. N. *Mössbauer Spectroscopy*; Chapman and Hall: London, 1971. Moore, M. F.; Wilson, S. R.; Cohn, M. J.; Dong, T.-Y.; Kampara, T.; Hendrickson, D. N. *Inorg. Chem.* **1985**, *24*, 4559−4565. (b) Dong, T.-Y.; Kampara, T.; Hendrickson, D. N. *J. Am. Chem. Soc.* **1986**, *108*, 5857−5865. Kampara, T.; Hendrickson, D. N.; Dong, T.-Y.; Cohn, M. J. *J. Chem. Phys.* **1987**, *86*, 2362. (c) Le Vanda, C.; Cowan, D. O.; Leitch, C.; Bechgaard, K. *J. Am. Chem. Soc.* **1974**, *96*, 6788−6789. (d) Le Vanda, C.; Bechgaard, K.; Cowan, D. O. *J. Org. Chem.* **1976**, *41*, 2700−2704.
(51) Dong, T.-Y.; Hendrickson, D. N.; Pierpont, C. G.; Moore, M. F. *J. Am. Chem. Soc.* **1986**, *108*, 963−971.
(52) Gütlich, P.; Link, R.; Trautwein, A. X. *Mössbauer Spectroscopy and Transition Metal Chemistry*; Springer−Verlag: Berlin, 1978; Vol. 3, p 280. Webb, R. J.; Geib, S. J.; Staley, D. L.; Rheingold, A. L.; Hendrickson, D. N. *J. Am. Chem. Soc.* **1990**, *112*, 5031−5042.
(53) Dong, T.-Y.; Sohel, C.-C.; Hwang, M.-Y.; Lee, T. Y.; Yeh, S.-K.; Wen, Y.-S. *Organometallics* **1992**, *11*, 573−582.
(54) Roué, S.; Lapinte, C.; Bataille, T. *Organometallics* **2004**, *23*, 2558−2567.
(55) Hamon, P.; Justaud, F.; Cador, O.; Hapiot, P.; Rigaut, S.; Toupet, L.; Ouahab, L.; Stueger, H.; Hamon, J.-R.; Lapinte, C. *J. Am. Chem. Soc.* **2008**, *130*, 17372−17383.
(56) Kahn, O. *Molecular Magnetism*; VCH Publishers: New York, 1993; p 380.
(57) Paul, F.; Bondon, A.; Da Costa, G.; Malvoti, F.; Sinbandit, S.; Cador, O.; Costuas, K.; Toupet, L.; Boillot, M.-L. *Inorg. Chem.* **2009**, *48*, 10608−10624.
(58) Sato, M.; Hayashi, Y. *Organometallics* **1996**, *15*, 721−728.
(59) Duff, C. M.; Heath, G. A. *Inorg. Chem.* **1991**, *30*, 2528−2535.
(60) The band expected for the dications in equilibrium with the MV complexes at ca. 5300 cm^{-1} was neglected. Indeed, because of the small molar fraction of the dication (maximum of 0.18), combined with the small extinction coefficient of the LF band, introduction of this component into the calculations did not significantly change the result of the fits.
(61) D'Alessandro, D. M.; Keene, F. R. *Chem. Rev.* **2006**, *106*, 2270−2298.
(62) Launay, J.-P.; Coudret, C.; Hortholary, C. *J. Phys. Chem. B* **2007**, *111*, 6788−6797.
(63) Frisch, M. J. T., G. W.; Schlegel, H. B.; Scuseria, G. E.; Robb, M. A.; Cheeseman, J. R.; Montgomery, Jr., J. A.; Vreven, T.; Kudin, K. N.; Burant, J. C.; Millam, J. M.; Iyengar, S. S.; Tomasi, J.; Barone, V.; Mennucci, B.; Cossi, M.; Scalmani, G.; Rega, N.; Petersson, G. A.; Nakatsuji, H.; Hada, M.; Ehara, M.; Toyota, K.; Fukuda, R.; Hasegawa, J.; Ishida, M.; Nakajima, T.; Honda, Y.; Kitao, O.; Nakai, H.; Klene, M.; Li, X.; Knox, J. E.; Hratchian, H. P.; Cross, J. B.; Bakken, V.; Adamo, C.; Jaramillo, J.; Gomperts, R.; Stratmann, R. E.; Yazyev, O.; Austin, A. J.; Cammi, R.; Pomelli, C.; Ochterski, J. W.; Ayala, P. Y.; Morokuma, K.; Voth, G. A.; Salvador, P.; Dannenberg, J. J.; Zakrzewski, V. G.; Dapprich, S.; Daniels, A. D.; Strain, M. C.; Farkas, O.; Malick, D. K.; Rabuck, A. D.; Raghavachari, K.; Foresman, J. B.; Ortiz, J. V.; Cui, Q.; Baboul, A. G.; Clifford, S.; Cioslowski, J.; Stefanov, B. B.; Liu, G.; Liashenko, A.; Piskorz, P.; Komaromi, I.; Martin, R. L.; Fox, D. J.; Keith, T.; Al-Laham, M. A.; Peng, C. Y.; Nanayakkara, A.; Challacombe, M.; Gill, P. M. W.; Johnson, B.; Chen, W.; Wong, M. W.; Gonzalez, C.; Pople, J. A. *Gaussian 03 Revision C02, and Gaussian 03, Revision C02*; Gaussian, Inc.: Wallingford CT, 2004.

(64) (a) Mielich, B.; Savin, A.; Stoll, H.; Preuss, H. *Chem. Phys. Lett.* **1989**, *157*, 200−206. (b) Lee, C.; Yang, W.; Parr, R. G. *Phys. Rev. B* **1988**, *37*, 785−788. (c) Becke, A. D. *J. Chem. Phys.* **1993**, *98*, 5648.
(65) Hay, P. J.; Wadt, W. R. *J. Chem. Phys.* **1985**, *82*, 270−299.
(66) *Jaguar 6.0*; Schrodinger, LLC: New York, 2005.
(67) Flükiger, P.; Lüthi, H. P.; Portmann, S.; Weber, J. *MOLEKEL4.3*; Swiss Center for Scientific Computing: Manno, 2002.
(68) (a) Roos, B. O.; Taylor, P. R.; Siegbahn, P. E. M. *Chem. Phys.* **1980**, *38*, 157−173. (b) Werner, H.-J.; P. J. Knowles, P. J. *J. Chem. Phys.* **1985**, *82*, 5053−5063. (c) Knowles, P. J.; Werner, H.-J. *Chem. Phys. Lett.* **1985**, *115*, 259−267.
(69) (a) Werner, H.-J.; Knowles, P. J. *J. Chem. Phys.* **1988**, *89*, 5803−5814. (b) Knowles, P. J.; Werner, H.-J. *Chem. Phys. Lett.* **1988**, *145*, 514−522.
(70) Werner, H.-J.; Knowles, P. J.; Knizia, G.; Manby, F. R.; Schütz, M.; Celani, P.; Korona, T.; Lindh, R.; Mitrushenkov, A.; Rauhut, G.; Shamasundar, K. R.; Adler, T. B.; Amos, R. D.; Bernhardsson, A.; Berning, A.; Cooper, D. L.; Deegan, M. J. O.; Dobbyn, A. J.; Eckert, F.; Goll, E.; Hampel, C.; Hesselmann, A.; Hetzer, G.; Hrenar, T.; Jansen, G.; Köppl, C.; Liu, Y.; Lloyd, A. W.; Mata, R. A.; May, A. J.; McNicholas, S. J.; Meyer, W.; Mura, M. E.; Nicklaß, A.; O'Neill, D. P.; Palmieri, P.; Pflüger, K.; Pitzer, R.; Reiher, M.; Shiozaki, T.; Stoll, H.; Stone, A. J.; Tarroni, R.; Thorsteinsson, T.; Wang, M.; Wolf, A. *MOLPRO: A Package of Ab Initio Programs*, see http://www.molpro.net.
(71) Hehre, W. J.; Stewart, R. F.; Pople, J. A. *J. Chem. Phys.* **1969**, *51*, 2657−2664.
(72) Connelly, N. G.; Geiger, W. E. *Chem. Rev.* **1996**, *96*, 877−910.
(73) Roger, C.; Hamon, P.; Toupet, L.; Rabaâ, H.; Saillard, J.-Y.; Hamon, J.-R.; Lapinte, C. *Organometallics* **1991**, *10*, 1045−1054.
(74) Otwinowski, Z.; Minor, W. Processing of X-ray Diffraction Data Collected in Oscillation Mode. In *Methods in Enzymology, Macromolecular Crystallography, Part A*; Carter, C. W, Sweet, R. M, Eds.; Academic Press: New York, 1997; Vol. *276*, pp 307−326.
(75) SMART & SAINT Software, Versions 5.611 and 6.45; Bruker AXS, Inc.: Madison, WI, 2003.
(76) CrysAlis RED, Version 1.171.26pre2 beta; Oxford Diffraction, Ltd.: Abington, U.K., 2004.
(77) Altomare, A.; Burla, M. C.; Camali, M.; Cascarano, G.; Giacovazzo, C.; Guagliardi, A.; Moliterni, A. G. G.; Polidori, G.; Spagna, R. *J. Appl. Crystallogr.* **1999**, *31*, 115−119.
(78) Sheldrick, G. M. *Acta Crystallogr., Sect. A: Found. Crystallogr.* **2008**, *A64*, 112−122.
(79) Reidel, D. *International Tables for X-ray Crystallography*; Kynoch Press: Birmingham, U.K., 1974; Vol. *IV*.
(80) Spek, A. L. *PLATON-98: A Multipurpose Crystallographic Tool*, Utrecht University: Utrecht, The Netherlands, 1998.